# Front page

**Exam information**
N510014102 - N510014102: SPFY801: Master's thesis in Physics, Johanna Müller

**Handed in by**
Johanna Müller
jomul23@student.sdu.dk

**Exam administrators**
Laura Ingeborg Davidsen
lauraid@sdu.dk
+4565509626

**Assessors**
Manuel Meyer
Examiner
mey@sdu.dk
+4565503654

Michael Kachelriess
Co-examiner
michael.kachelriess@ntnu.no
+4799890701

**Hand-in information**

**Title:** Investigating the origin of multi TeV emission of the GRB 221009A
**Title, english:** Investigating the origin of multi TeV emission of the GRB 221009A
**Does the hand-in contain confidential material:** Yes
**May the handin be subject of lending:** Yes
**May handin be used for teaching:** Yes

SDU

Master Thesis in Physics

# Investigating the origin of multi TeV emission of the GRB 221009A

Spring and Autumn Semester 2024

Student: Johanna Müller
Adress: Niels Bohrs Alle 23 1.1141, 5230 Odense M, Denmark
Student ID: 4120698
Date of submission: 01.01.2025

University of Southern Denmark
Department of Physics, Chemistry and Pharmacy
Odense, Denmark

Supervisor: Professor Manuel Meyer

# Abstract

Gamma-ray bursts (GRBs) are among the brightest phenomena observed in the Universe. In October 2022, the brightest GRB ever recorded, GRB 221009A, was observed across the electromagnetic spectrum, with energies reaching up to 13 TeV.
Leptonic models explain the gamma-ray emission of these events through the emission of gamma rays from accelerated electrons. The main gamma-ray production mechanisms are inverse Compton scattering or synchrotron self-Compton processes. However, leptonic models alone might not be sufficient to explain the emission above 10 TeV, suggesting that ultrahigh-energy cosmic rays could be involved.
All particles, that escape a GRB can potentially scatter with background electromagnetic fields, such as the cosmic microwave background or the extragalactic background light, and produce electromagnetic cascades. These cascades can then contribute to the observed gamma-ray flux.
This thesis investigates whether proton-initiated cascade emissions can effectively explain the very high energy gamma-ray emission of GRB 221009A. To achieve this, numerical simulations along with observational data are used. The Monte Carlo simulation code CRPropa makes it possible to simulate proton-initiated electromagnetic cascades in randomized magnetic fields and obtain the spectrum created by them.
The simulation results are then used to constrain the proton-induced cascade emission by comparing the simulation data with the observational data. For that I use data from LHAASO directly after the GRB. Using the python package iminuit and chi-squared statistics, parameter limits for the intrinsic gamma-ray and the proton spectrum, are derived.
The deflection of gamma-ray emitting charged particles by intergalactic magnetic fields increases their path to Earth, resulting in a time delay for some gamma-ray emissions. For that reason, later observation times are also considered. In particular, I analyse data from the Fermi LAT telescope 2-9 days after the GRB and use them together with contemporaneous data from HESS to compare the expected cascade emission with the observational limits.
The simulations also provide a flux of neutrino originating in the decay of pions, produced in photopion processes between protons and background radiation fields. By comparing the simulated neutrino flux to the upper limit from the non-observation of neutrinos by IceCube further constraints can be obtained.

# Resumé

Gammastråle udbrud (GRBs) er blandt de mest lysstærke fænomener, der er observeret i Universet. I Oktober 2022 blev det lyseste GRB, som nogensinde er registreret, GRB 221009A, observeret over hele det elektromagnetiske spektrum med energier op til 13 TeV.

Leptoniske modeller forklarer udsendelsen af gammastråler fra disse begivenheder gennem udsendelse af gammastråler fra accelererede elektroner. De primære mekanismer i produktionen af gammastråler er invers Compton-spredning eller synkrotron selv-Compton processer. Leptoniske modeller er dog ikke alene tilstrækkelige til at forklare emission over 10 TeV, hvilket tyder på, at kosmiske stråler med ultrahøj energi kan være involveret.

Alle partikler, der undslipper en GRB, kan potentielt spredes med elektromagnetiske felter i baggrunden, såsom den kosmiske mikrobølgebaggrund eller det ekstragalaktiske baggrundslys og producere elektromagnetiske kaskader. Disse kaskader kan bidrage til den observerede gammastråleflux.

Denne afhandling undersøger, om proton-initierede kaskade emissioner kan forklare den meget højenergiske gammastråling fra GRB 221009A effektivt. For at opnå dette benyttes numeriske simulationer sammen med observeret data. Monte Carlo simulations koden CRPropa muliggør at simulere proton-indledte elektromagnetiske kaskader i tilfældiggjorte magnetiske felter og få det spektrum der skabes af dem.

Simuleringsresultaterne bruges derefter til at begrænse den protoninducerede kaskadeemission ved at sammenligne simuleringsdataet med den observerede data. Til det bruger jeg data fra LHAASO, direkte efter GRB'en. Ved at anvende python pakken iminuit og chi-i-anden statistikker udledes parametergrænser for den intrinsiske gammastråle- og protonspektrum.

Afbøjningen af ladede partikler, der udsender gammastråler, af intergalaktiske magnetfelter øger deres vej til Jorden, hvilket resulterer i en tidsforsinkelse for nogle gammastråler. Af den grund er senere observationstider også taget i betragtning. Jeg analyserer især data fra Fermi LAT-teleskopet 2-9 dage efter GRB'en, og bruger dem sammen med samtidige data fra HESS til at sammenligne den forventede kaskadeemission med observationsgrænserne.

Simuleringerne giver også en flux af neutrinoer, der stammer fra henfaldet af pioner, som produceres i fotopion processer mellem protoner og baggrundsstrålingsfelter. Ved at sammenligne den simulerede neutrino-flux med den øvre grænse fra IceCubes manglede observationer af neutrinoer kan der opnås yderligere begrænsninger.

## Statutory Declaration

I hereby declare that I have written this thesis independently and without the use of sources and aids other than the cited sources. Sentences, parts of sentences and thoughts taken directly or indirectly from external sources are marked as such. This work has neither been submitted in the same or similar form to any other examination body nor published. This work has not been used, not even in part, in another examination or as a course assignment.

Hage, January 1, 2025

Johanna Müller

# Acknowledgements

I would like to express my sincere thanks to all those who have supported me in various ways during the completion of this thesis.

First, I would like to thank Manuel Meyer for making this thesis possible, as well as for providing invaluable guidance and feedback. You have been a great supervisor. I also want to thank Atreya Acharyya for his mentorship and for always keeping his door open for my questions.

Furthermore, I would like to thank everyone in the Axion-ALP-DM group, both at SDU and in Hamburg, and everyone at the CP3 center at SDU for their support and advice.

A special thanks goes to Matthias Hübl, Atreya Acharyya and Eike Ravensburg for proofreading this thesis and to Katrine Jacqueline Vølund Kennedy for helping me translate the abstract into Danish.

Finally, I want to thank my family and friends for their continuous support throughout my thesis.

# Contents

**Abbreviations** **7**

**1 Introduction** **8**

**2 Gamma-ray bursts** **9**
2.1 GRB phenomenology . . . . . 9
2.1.1 Classification . . . . . 10
2.2 GRB progenitors and hosts galaxies . . . . . 10
2.3 Theoretical model of GRBs . . . . . 11
2.3.1 The fireball model . . . . . 11
2.3.2 The internal shock model . . . . . 12
2.3.3 The afterglow emission . . . . . 13
2.4 High energy emission from GRBs . . . . . 15
2.4.1 Leptonic processes . . . . . 15
2.4.2 Hadronic processes . . . . . 19
2.5 Extragalactic background light . . . . . 21

**3 Particle cascades from gamma-ray bursts** **23**
3.1 Cascade emission origin . . . . . 23
3.2 How cascade emission can explain high-energy emission . . . . . 23
3.3 Cascade emission from prompt emission of GRB 221009A . . . . . 25

**4 Detection of GRBs** **26**
4.1 Gamma-ray detection . . . . . 26
4.1.1 HESS . . . . . 27
4.1.2 LHAASO . . . . . 28
4.1.3 Fermi LAT . . . . . 29
4.2 Detection of Neutrinos . . . . . 30
4.2.1 IceCube . . . . . 31

**5 GRB 221009A** **32**
5.1 Detection of GRB 221009A . . . . . 32

5.1.1 The LHAASO data . . . . . 33
5.1.2 The HESS data . . . . . 34
5.1.3 Fermi LAT data . . . . . 34

**6 Constraining the cascade contribution of GRB 221009A 39**
6.1 Simulating cascades using CRPropa . . . . . 39
6.2 Comparing with LHAASO data . . . . . 41
6.2.1 Determining a limit for the cascade contribution . . . . . 43
6.3 Comparing with limits from IceCube . . . . . 47
6.4 Late time observation . . . . . 49

**7 Summary & Outlook 52**

**Bibliography 54**

**A Appendix 60**
A.1 Comparing to LHAASO data . . . . . 60

# Abbreviations

**CMB** Cosmic Microwave Background

**EBL** Extragalactic Background Light

**EGMF** Extragalactic Magnetic Field

**GRB** Gamma-Ray Burst

**IACT** Imaging Atmospheric Cherenkov Telescopes

**ISM** Interstellar Medium

**PSF** Point Spread Function

**SED** Spectral Energy Distribution

**UHECR** Ultra-High-Energy Cosmic Ray

# Chapter 1

# Introduction

The first Gamma-ray burst (GRB) was detected by accident in the 1960s by the Vela satellites, which were monitoring the adherence of the nuclear test ban. Since this first detection of a GRB, several other GRBs have been observed, and with the development of new technologies more and more features of these phenomena can be studied. This also led to the separation of short GRBs with a duration below 2 s and long GRBs with a duration above 2 s (Kouveliotou et al., 1993).
Today many different satellites and earth-bound observatories, covering a broad range of the electromagnetic spectrum together with giant neutrino observatories are looking for signals from GRBs.
One special GRB was the GRB 221009A, which this thesis focuses on. It is until now the brightest GRB ever recorded. Additionally, the detection of photons with energies up to 13 TeV makes it the first GRB observed at these high energies (Cao et al., 2023a). The emission of GRBs is usually explained by leptonic models, explaining the gamma-rays as emission from accelerated electrons. However, these models have problems explaining the energies above 10 TeV, as the emitted gamma ray at these energies suffer from strong attenuation by interacting with photons from the extragalactic background light (EBL) (Das et al., 2023).
Proton-induced cascades, which will be studied in this work, are a possible mechanism for explaining these high energy emissions.

The thesis is structured in the following way: In chapter 2, the theoretical model of GRBs and the involved physical processes are explained. In the following chapter 3 the proton-induced cascades are discussed. Afterwards, in chapter 4 the different used observatories are introduced, followed by a chapter about the observation of GRB 221009A using them. Chapter 6 presents the results found during this project, which are then summarized in chapter 7.

# Chapter 2

# Gamma-ray bursts

## 2.1 GRB phenomenology

GRBs are bright bursts of gamma rays, with typical photon energies of tens of keV up to several MeV, but sometimes even with photon energies up to $> 100$ GeV (Zhang, 2018). GRBs show a great variation in their light curves, but their emissions can be roughly described by two phases: The early, bright prompt emission, followed by the fainter afterglow. Sometimes also a precursor, an early increase of the photon flux, much smaller than the main emission, can be observed. The prompt emission typically shows a broad variability, and can consist of several peaks, whereas the afterglow is characterized by a smooth exponentially decaying emission.
Figure 2.1 shows the light curve of the discovery of GRB 221009A with the Fermi Gamma-ray Burst Monitor (GBM) without corrections for pileup effects and the instrument response function. The light curve shows a precursor at $t = 0$ s, the prompt emission phase and the afterglow after $t = 600$ s.

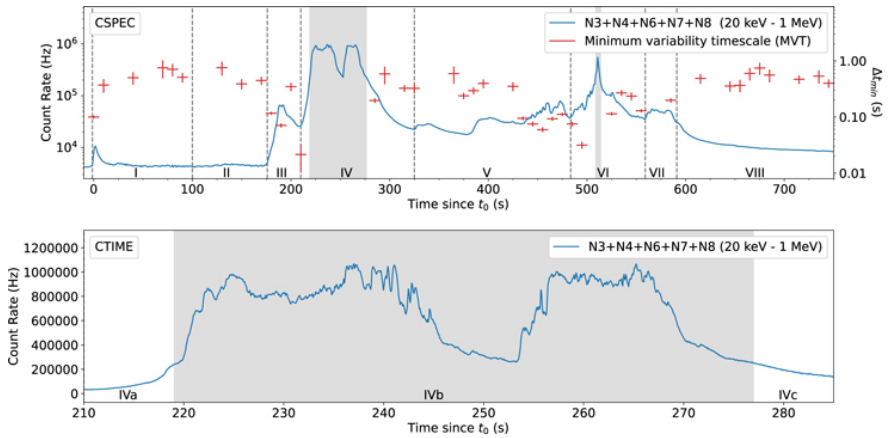


Figure 2.1: GRB 221009A lighthcurve with Fermi GBM (Lesage et al., 2023)

### 2.1.1 Classification

The observed light curves of GRBs generally depend on the used detectors, as they have different energy ranges and sensitivities, but in general GRBs can be classified using their duration. An useful tool is the $T_{90}$ time interval, that is the time between the moment when 5% and 95% of all energy has been emitted (Zhang, 2018). According to Kouveliotou et al. (1993) one can differentiate short GRBs with a duration of less that two seconds and long GRBs with a duration above that. The logarithmic mean of the $T_{90}$ for the two populations is around $0.33\ \mathrm{s} \pm 0.21\ \mathrm{s}$ and $26.2\ \mathrm{s} \pm 1.7\ \mathrm{s}$.

## 2.2 GRB progenitors and hosts galaxies

The progenitors of GRBs are the key to understanding these extraordinary phenomena better. The host galaxies and the GRBs location within them give insights into the progenitors, the conditions necessary for these events, and their environment.

**Short gamma ray bursts** are thought to be the result of the collision of two compact objects, namely the merger of two neutron stars or a neutron star and a black hole (Zhang, 2018). When these objects merge gravitational waves are emitted. In 2017 the gravitational wave event GW170817, emitted by the merger of two neutron stars, was associated with a short GRB (Abbott et al., 2017). This observation supports the current model, but remains the only detection so far.
Further, indirect support for the model comes from the location of short GRBs within their host galaxies. A study conducted using the Hubble telescope by Fong et al. (2013) examined the short GRB population and found that short GRBs exist in elliptical and disk-like galaxies. In addition, they measured that short GRBs have an offset 3.5 times larger from their host galaxy center than long-duration bursts. Additionally, short GRBs are observed in faint UV and optical regions of their host galaxy. Bright regions often coincide with areas of active star formation, where it is especially likely to find massive stars, which are the progenitors of objects, such as neutron stars. Fong et al. (2013) therefore argue that finding short GRBs in these fainter regions and with larger offset from their host galaxy center support the compact merger model as neutron stars or black holes are thought to be ejected from their birth sites when they are formed.

**Long gamma ray bursts** are linked to the death of massive stars, particularly to core-collapse supernovae. Especially they often are associated with Type Ic supernovae, as they show similar spectral features (Zhang, 2018).
In comparison to short GRBs a study by Fruchter et al. (2006) found that the majority of long GRBs are located in irregular galaxies. Within those long GRBs tend to be located in the brightest regions. Bright regions often coincide with areas of active star

formation, where it is especially likely to find massive stars, which supports the massive star origin of long GRBs. Although all GRBs that were spectroscopically associated with supernovae were associated with Type Ic supernovae, only a very small fraction of Type Ic supernova is associated with GRBs (Zhang, 2018). This discrepancy gives rise to the question what special conditions are necessary for a core-collapse supernova to become a GRB. There are many different hypotheses; one of them is the difference in metallicity (Fruchter et al., 2006) but the question still remains open until today.

## 2.3 Theoretical model of GRBs

The canonical theoretical model of GRBs can be, according to Zhang (2018), divided into three different stages: a catastrophic event, a prompt emission and an afterglow. As mentioned in section 2.2, long GRBs are associated with the death of massive stars, whereas short GRBs are associated with the merger of a neutron star with another neutron star or a neutron star with a black hole. These events lead to the formation of a central engine, which is thought to be a stellar-sized black hole or a rapidly rotating neutron star, called a magnetar. This central engine powers a collimated and highly relativistic outflow, made out of photons, leptons and bayons, referred to as jet. During the prompt emission phase, the internal energy of leptons, and depending on the model, also baryons, is radiated away in non-thermal emission. The final phase is the afterglow, which is thought to arise when the jet interacts with the surrounding medium and decelerates. This evolution of the GRB is illustrated in figure 2.2.

### 2.3.1 The fireball model

A widely used model to describe the evolution of the launched jet is the photon-lepton fireball (Goodman, 1986, Paczynski, 1986). In their model, a short-duration sudden release of energy can lead to the creation of a fireball where photons, electrons and positrons are in thermal equilibrium. Additionally Shemi et al. (1990) considered the possibility of baryonic loadings, meaning that the fireball also contains a fraction of baryons, i.e. protons and neutrons.
Following the review on the fireball model by Piran (1999) the fireball evolution is described as follows. If the initial temperature is high enough positron-electron pairs are created and the fireball is optically thick. As the fireball expands, energy is conserved, causing an increase in the bulk Lorentz factor (for a detailed calculation see Zhang, 2018), whereas the local temperature drops and eventually lies below the pair-creation threshold so that the photons are able to escape. From this model, thermal radiation is expected, which does not reflect the non-thermal emission observed in GRBs prompt

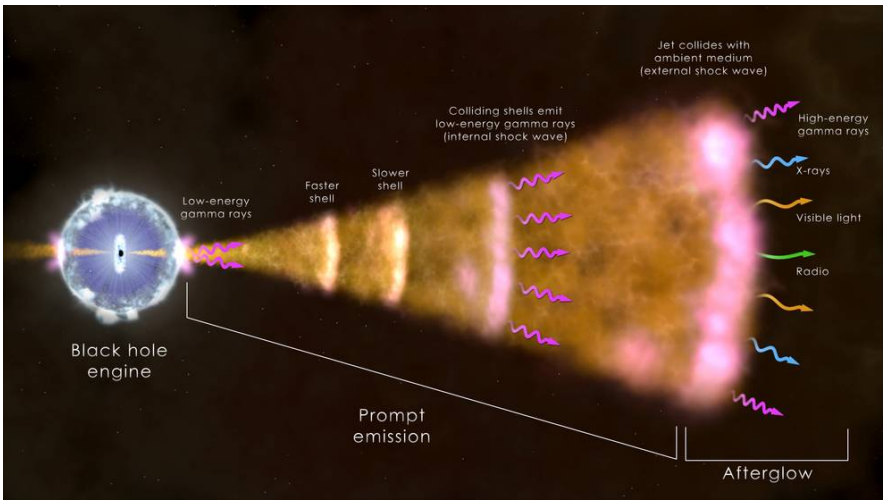


Figure 2.2: The picture shows the theoretical evolution of a GRB in the internal-external shock model. The launched jet is initially opaque and, later at the photosphere, becomes optically thin to the photons. In the internal shock model the prompt emission is produced by colliding shells within the jet. The external shock model explains the final stage of the GRB, the afterglow, by the jet interacting with the surrounding medium. (NASA's Goddard Space Flight Center, n.d.)

emission. However, it explains how the leptons and baryons obtain their initial kinetic energy. The fireball might also contain some baryons that could be injected at the beginning or come from the atmosphere. These baryons are then accelerated together with the leptons and increase the optical depth, delaying the moment when the fireball becomes optically thin.

### 2.3.2 The internal shock model

One of the main questions is how the relativistic kinematic energy form the leptons and baryons during the prompt emission phase is converted to radiative energy and how the irregular light curve is created (Kumar et al., 2015). This is where the internal shock model for the prompt emission steps in. The following section describing this model follows the review by Kumar et al. (2015).

In the internal shock model, collision of shells with different Lorentz factors are responsible for converting kinetic energy to radiation. The strength of the model is that it can explain the observed variability time scale.

Consider two shells of masses $m_1$ and $m_2$, and Lorentz factors $\Gamma_1$ and $\Gamma_2$, respectively. Suppose that $\Gamma_2 > \Gamma_1$ and that the second shell is emitted at $t_0$ and the slower moving shell 1 a time difference $\delta t$ before that. The radius $R_{coll}$, where the shells collide is given by (Kumar et al., 2015):

$$R_{coll} = \frac{v_1 v_2 \delta t}{v_2 - v_1} \approx 2c\Gamma_1^2 \delta t, \tag{2.1}$$

where $v_1$ and $v_2$ are the velocities of the shells. Therefore the time an observer sees the collision is at (Kumar et al., 2015):

$$t_{obs} \approx t_0 + \frac{R_{coll}}{2c\Gamma_f^2} \approx t_0 + \delta t \frac{\Gamma_1}{\Gamma_2}, \tag{2.2}$$

where $\Gamma_f$ is the Lorentz factor of the merged shells. Consequently the observed flux variability directly connects with the variability time of the central engine. Although the internal shock model describes the observed variability seen in GRBs prompt emission very well, a problem of this theory is the efficiency, given by (Kumar et al., 2015):

$$\epsilon_t = 1 - \frac{m_1 + m_2}{\sqrt{m_1^2 + m_2^2 + 2m_1 m_2 \Gamma_r}}, \tag{2.3}$$

where $\Gamma_r = \Gamma_1 \Gamma_2 (1 - \frac{v_1 v_2}{c^2})$ is the relative Lorentz factor between the shells before the collision. Most of the energy in these collisions goes into magnetic fields and the protons, whereas only a fraction is kept in electrons. Since protons are very inefficient radiators they can reach much higher energies in these collisions. At the same time, they also reduce the radiation efficiency. The maximal efficiency that can be reached in these collisions is obtained when equal mass shells of very different Lorentz factor collide and is expected to be way lower than the efficiency suggested by observations. Nevertheless, the internal shock mechanism provides us with accelerated particles that can than radiate through different processes. Electrons can emit synchrotron radiation or scatter in inverse Compton processes. Protons could contribute to the gamma-ray flux through photo-pion processes or Bethe-Heitler processes, when they scatters with photons. In photo-pion processes a pion is produced by the interaction of the proton with a photon. These pions can either be $\pi^0$, which directly decay into gamma-rays or charged pions that decay into muons. In Bethe Heitler processes an electron-positron pair is created, that can afterwards produce gamma-rays through inverse Compton scattering with background radiation fields. These processes will be explained in more detail in section 2.4.2.

### 2.3.3 The afterglow emission

The afterglow of GRBs is thought to arise when the jet interacts with the external interstellar medium (ISM) and decelerates (Piran, 1999). When the jet collides with the ISM, a forward and a reverse shock are formed, which are separated by a contact discontinuity (Piran, 2005). These shock waves can accelerate particles through diffusive shock acceleration resulting in a power-law distribution of the electrons behind the shock wave. They can also create reasonably strong magnetic fields (Sari et al., 2001).

Sari et al. (2001) studied the evolution of the afterglow produced by synchrotron self-Compton processes in the GRB. They argue that due to the stronger magnetic fields created by the shock wave, the electrons produce synchrotron radiation, which can serve as seed-photons for inverse Compton scattering. Therefore, the afterglow emission ranges from radio to gamma-ray energies.

Absorption lines in the afterglow are typically used to determine the redshift of the gamma-ray burst. For GRB 221009A de Ugarte Postigo et al. (2022) detected the absorption lines of Ca II, Ca I, and Na I D, and used this to determine a redshift of $z = 0.151$.

During the afterglow also the cone-shaped structure of the jet is revealed, characterized by the jet break, as shown in figure 2.3. Due to relativistic beaming, only the emission within an angle of $\theta \propto \frac{1}{\Gamma}$, where $\Gamma$ is the bulk-Lorentz factor, can be observed (Zhang, 2018). When this angle widens due to the deceleration of the jet, through the interaction with the ISM, it will at some point become larger than the jet opening angle. As there is no emission beyond the jet cone, the brightness evolution of the burst becomes softer with time, see figure 2.3.

This jet break was also observed for GRB 221009A by Cao et al. (2023b) and a half-opening angle of 0.8° was determined.

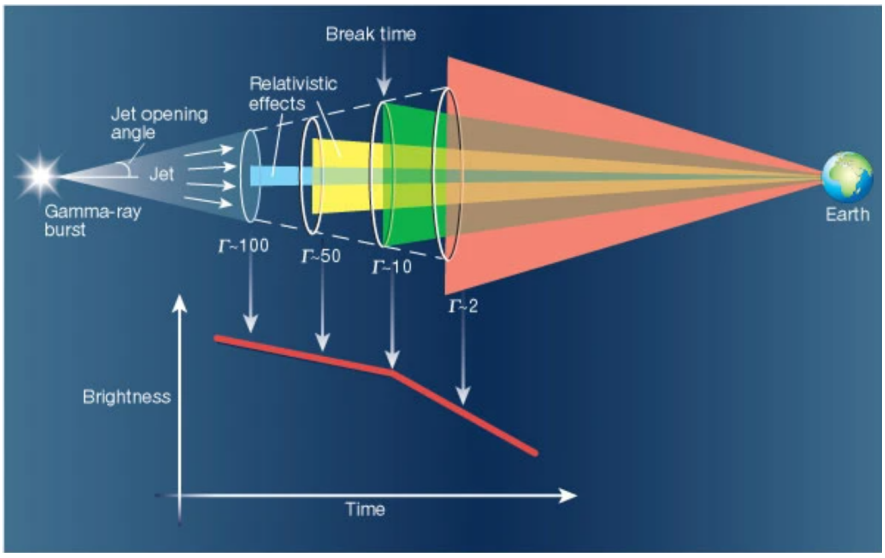


Figure 2.3: The picture shows how the jet break becomes apparent during the afterglow of a GRB. (Woosley, 2001)

## 2.4 High energy emission from GRBs

Radiative processes such as synchrotron radiation, Inverse Compton scattering as well as hadronic processes like pion production are essential processes in gamma-ray bursts to produce the observed high-energy photons.
To generate high-energy photons using these processes, a distribution of high-energy electrons respectively protons is required. An example of a process capable of accelerating particles to high energies is Fermi acceleration by shock waves.

### 2.4.1 Leptonic processes

#### Compton and inverse Compton scattering

Compton scattering describes the scattering of a photon with a charged particle, typically an electron, see figure 2.4. There are two types of scattering, depending on

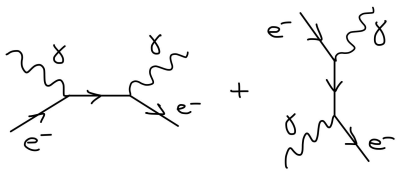


Figure 2.4: Lowest order Feynman diagrams of Compton scattering

whether the electron or the photon gains energy (Ghisellini, 2013). The first process is direct Compton scattering, whereas the latter is inverse Compton scattering.
In the following section, inverse Compton scattering will be discussed in greater detail, as it plays a crucial role in producing high-energy gamma rays in GRBs.
According to Ghisellini (2013) there are two distinct limits of inverse Compton scattering. In the Thomson limit, the photon energy before scattering $\epsilon_0'$ in the electrons reference frame $K'$ is much smaller than the electron's rest mass $m_e c^2$. In this case the classical scattering cross section can be used, and the recoil of the electron can be neglected. On the other hand, in the Klein-Nishina regime, when $\epsilon_0' \gg m_e c^2$, the recoil and quantum corrections to the cross section must be considered and the cross-section becomes energy dependent.

**Energy gain in Thomson limit** To get an idea of how much energy can be gained in inverse Compton processes it is helpful to discuss the energy gain in the Thomson limit. Considering highly energetic electrons with Lorentz factor $\gamma$ and photons with initial energy $\epsilon$ in the lab frame $K$, the maximal photon energy after scattering in the

lab frame is $\epsilon_{1,max} \approx 4\gamma^2\epsilon$ for head-on collisions and the minimal energy achieved in a tail-on collision is $\epsilon_{1,min} \approx \frac{\epsilon}{4\gamma^2}$ (Blumenthal et al., 1970). The difference between head-on and tail-on collisions is shown in figure 2.5. The maximal energy achievable in these collisions shows, that the seed photons can be scattered to very high energies during inverse Compton scattering.

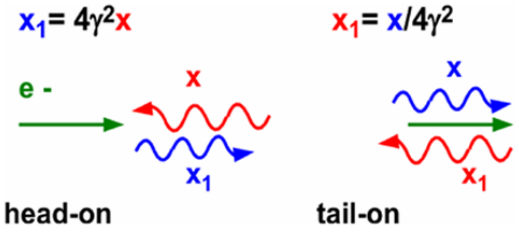


Figure 2.5: Head-on collisions and tail-on collisions observed in the lab frame. (Ghisellini, 2013)

**The inverse Compton spectrum** The spectrum of a scattering process describes the number of photons, found at a given energy, after the scattering. Because the initial photons and electrons follow a given distribution one has to integrate over the photon energies $\epsilon$ and the electron distribution gamma factors $\gamma$ (Blumenthal et al., 1970):

$$\frac{dN_{tot}}{dtd\epsilon_1} = \int\int N_e(\gamma)d\gamma \left(\frac{dN_{\gamma,\epsilon}}{dtd\epsilon_1}\right), \tag{2.4}$$

where $\epsilon_1$ is the energy of the photons after scattering in the lab frame. An example of the obtained spectra for a monochromatic radiation field is shown in figure 2.6.

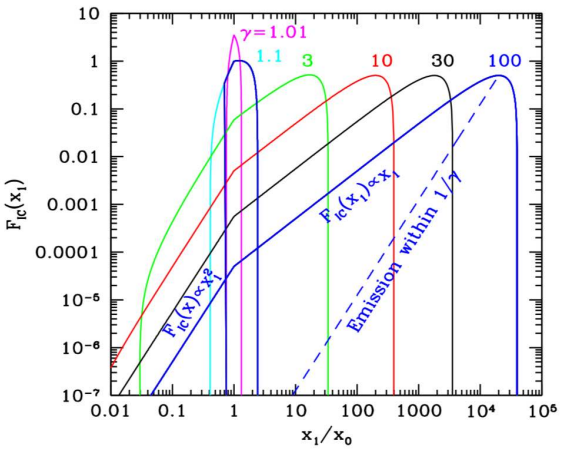


Figure 2.6: Inverse Compton spectrum emitted by scattering of monochromatic radiation on electrons of different $\gamma$, where $x_1$ is the photon energy after and $x_0$ before scattering. (Ghisellini, 2013, p. 79)

Figure 2.7 shows the normalized photon distribution after Compton scattering for different domains $\Gamma_\epsilon$ of the scattering. In the Thomson limit $\Gamma_\epsilon \ll 1$ the distribution peaks at low energies after scattering, whereas in the Klein-Nishina limit, with $\Gamma_\epsilon \gg 1$ the distribution peaks at high energies. Therefore the electron loses only a very small part of its energy in the Thomson limit, whereas in the Klein-Nishina limit the electrons lose a large fraction of their energy in a single scattering. The cross section (Blumenthal et al., 1970):

$$\sigma_{tot} \approx \sigma_T \left(1 - \frac{2\epsilon'}{mc^2} + ...\right), \tag{2.5}$$

shows that, the scattering is less likely to happen for high-energy photons than for low-energy photons, because the scattering cross section is lower in the Klein-Nishina regime, than in the Thomson limit.

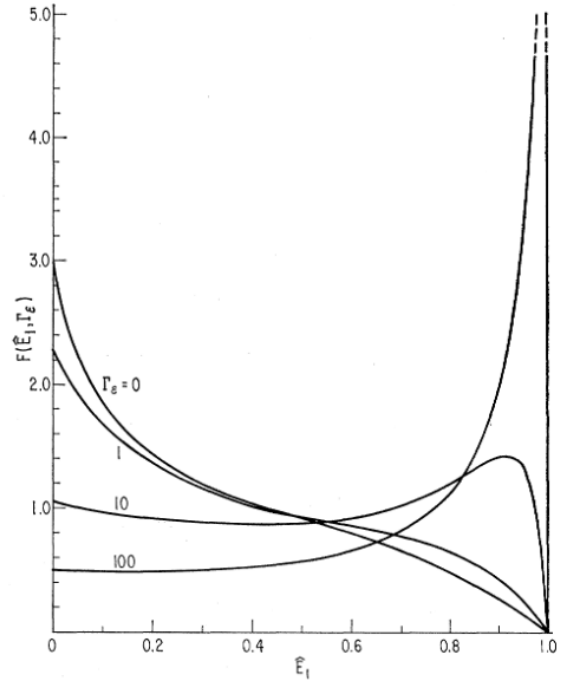


Figure 2.7: Normalized photon spectrum after Compton scattering for different domains of scattering $\Gamma_\epsilon = \frac{4\epsilon\gamma}{mc^2}$ as a function of the energy in parts of the maximal energy of the scattered photon $\hat{E}_1$ ranging from 0 to 1. (Blumenthal et al., 1970)

### Synchrotron radiation

Whenever an electrically charged particle gets deflected in a magnetic field, synchrotron radiation is emitted. The power per unit angle emitted by a relativistic electron in the

direction $\vec{n}$ is given by (Jackson, 1962 in Blumenthal et al., 1970):

$$\frac{dP(t)}{d\Omega_n} = \frac{e^2}{4\pi c} \frac{\left|\vec{n} \times [(\vec{n} - \vec{\beta}) \times \dot{\vec{\beta}}]\right|^2}{(1 - \vec{n} \cdot \beta)^6}, \tag{2.6}$$

where $\beta$ is the electrons velocity in the laboratory frame. To obtain the spectrum, the Fourier transform needs to be calculated. The detailed calculation can be found in Blumenthal et al., 1970. The synchrotron spectrum of a single electron is given by (Blumenthal et al., 1970):

$$P(\nu) = \frac{\sqrt{3} e^3 B}{mc^2} \frac{\nu}{\nu_{crit}} \int_{\nu/\nu_{crit}}^{\infty} K_{5/3}(x) dx, \tag{2.7}$$

where K is the Bessel function and $\nu_{crit}$ is the critical frequency, which is defined by $\frac{3eB\gamma^2}{4\pi mc}$, around which the distribution peaks.

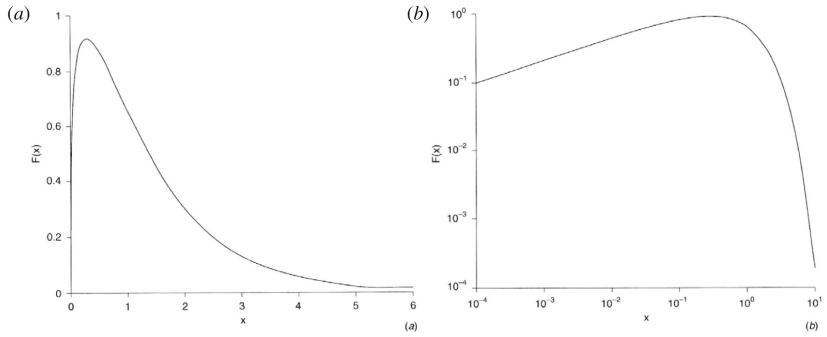


Figure 2.8: Synchrotron radiation of a single electron, where $x = \frac{\nu}{\nu_{crit}}$ in a with linear and b with logarithmic axis. (Longair, 2011)

Figure 2.8 shows the spectrum of synchrotron radiation. For small frequencies the spectrum can be approximated by a power law $\propto x^{1/3}$, whereas for high frequencies with $\propto x \cdot e^{-x}$ (Blumenthal et al., 1970).
Important to mention is also that synchrotron radiation is beamed in the particle's direction of movement. That means that most of the radiation is emitted within an angle of $\frac{1}{\gamma}$ of the direction of the electron's motion (Longair, 2011). This beaming causes the synchrotron light to be seen by the observer as pulses.
To obtain the synchrotron spectrum emitted by a distribution of electrons it is necessary to integrate over all electron contributions at a certain wavelength. For an electron distribution following a power law with index $p$, the one obtained synchrotron spectrum also follows a power law, but with index of $(p-1)/2$ (Longair, 2011).

### 2.4.2 Hadronic processes

In lepto-hadronic models of GRBs, both leptonic and hadronic processes are responsible for the emission of high-energy photons. In the following, I will focus specifically on the possible interactions of protons, as I will later study the cascade emission produced by protons escaping GRBs. The most important emission processes for protons are Bethe-Heitler and photopion production. Protons can also emit synchroton radiation, but due to its much larger mass compared to electrons they are very inefficient synchrotron emitters, and therefore I will not discuss this in detail.

#### Photopion production

In photopion processes, a pion is produced. There are four different processes contributing to the photopion cross section: resonant production, direct production, multipion production and diffractive scattering through vector mesons (Dermer et al., 2009, Chapter 9).
The most important resonant process is the one producing a $\Delta^+$ baryon (Dermer et al., 2009):

$$p + \gamma \rightarrow \Delta^+ \rightarrow \begin{cases} \pi^0 + p \\ \pi^+ + n \end{cases} , \tag{2.8}$$

and the most important direct production channel is

$$p + \gamma \rightarrow n + \pi^+. \tag{2.9}$$

Another main interaction process is the multipion production (Cerruti, 2020):

$$p + \gamma \rightarrow p + \pi^+\pi^- \tag{2.10}$$

The produced pions decay afterwards, with the main decay channels being (Cerruti, 2020):

$$\pi^0 \rightarrow 2\gamma \tag{2.11}$$

$$\pi^+ \rightarrow \mu^+ + \nu_\mu \rightarrow e^+ + \nu_e + \bar{\nu_\mu} + \nu_\mu \tag{2.12}$$

$$\pi^- \rightarrow \mu^- + \nu_\mu \rightarrow e^- + \bar{\nu_e} + \nu_\mu + \bar{\nu_\mu}. \tag{2.13}$$

The detection of neutrinos from GRBs would therefore be a clear signal for the presence of high energy protons and hence the validity of GRBs models that include a baryonic loading.
Depending on the process, the protons lose only a fraction or a major part of their

energy. For example in the single-pion resonance, where only one pion is produced the protons lose on average 20% of their energy, in comparison to the multipion-channel, where they lose on average 60% (Dermer et al., 2009).
The photopion production process gives an upper energy cutoff for proton energies, the Greisen–Zatsepin–Kuzmin (GZK) limit. It is caused by the interaction of high energy protons with the photons from the CMB. As the photopion production has a very high energy threshold, very highly energetic protons are necessary for the process to happen. Therefore this process has a neglectable effect on the proton spectrum below energies of $3 \cdot 10^{19}$ eV, but as the cross section rapidly increases above the energy threshold, it leads to the GZK cutoff around $1 \cdot 10^{20}$ eV (Greisen, 1966).
The necessary energy of the protons for photopion production can be reduced by higher energies of the scattering photons. The energy density of the optical interstellar radiation is by a factor of $5 \cdot 10^4$ smaller than the energy density of the Cosmic Microwave Background (CMB) (Greisen, 1966). Hence, the contribution to the gamma-ray flux by the proton scattering with these radiation is neglectable (Greisen, 1966).
Overall we can conclude that the photopion production only plays a minor role for the production of gamma-rays from proton-background light interactions below $10^{20}$ eV.

### Photopair production

In the photopair production an electron-positon pair is created by the scattering of a proton and a photon (Dermer et al., 2009):

$$p + \gamma \rightarrow p + e^- + e^+. \tag{2.14}$$

The created electrons and positrons can create electromagnetic cascades for example by inverse Compton scattering with the background electromagnetic radiation fields. Photopair production has an energy threshold that is a factor of 0.004 smaller than the photopion production (Cerruti, 2020). Therefore this process is the dominant mechanism for the creation of gamma-rays in proton interactions with electromagentic background fields below the GZK-cutoff. The energy loss as function of the protons energy for the two processes is shown in figure 2.9. In chapter 6, when studying the cascade contribution to GRB 221009A, we inject only protons in the energy range from $10^{12}$eV to $10^{18}$eV. Consequently, the dominating gamma-ray production process will be photopair processes.

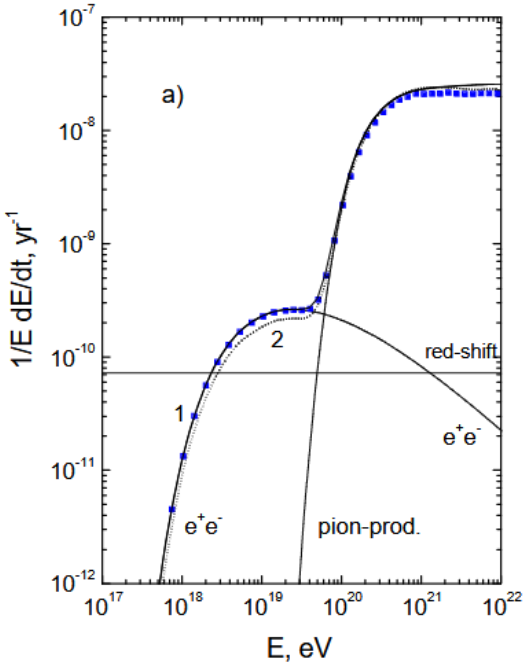


Figure 2.9: Energy loss as function of the protons energy (Berezinsky et al., 2006)

## 2.5 Extragalactic background light

The EBL is the electromagnetic radiation from resolved and unresolved extragalactic sources between $0.1 - 1000$ $\mu$m, with the exemption of the CMB and therefore is the accumulated light emitted since the epoch of recombination (Dwek et al., 2013). Figure 2.10 shows the spectral energy distribution of the EBL at $z = 0$ assuming the EBL model by Saldana-Lopez et al. (2021).

The EBL is crucial for understanding the spectra of high-energy photon sources, as high-energy photons are strongly attenuated through interactions with the EBL, since the intrinsic gamma-ray flux, originally emitted by a source, is attenuated exponentially. The observed flux $F_{obs}$ at an energy $E$ is given by (Dwek et al., 2013):

$$F_{obs}(E) = F_{int} \cdot e^{\tau_{\gamma\gamma}(E)}. \tag{2.15}$$

These interactions of gamma-rays lead to the production of an electron-positron pair, which can further initiate electromagnetic cascades. The optical depth of an observed photon at an energy E is given by (Dwek et al., 2013):

$$\tau_{\gamma\gamma}(E,z) = \int_0^z dz' \, \frac{dl}{dz'} \int_1^{-1} d\mu \, \frac{1-\mu}{2} \int_{\epsilon'_{th}}^{\infty} d\epsilon \, n_\epsilon(\epsilon, z') \, (1+z')^3 \, \sigma_{\gamma\gamma}(z', \beta'), \tag{2.16}$$

where $\epsilon'_{th}$ is the threshold energy for electron positron pair production, $z$ is the redshift

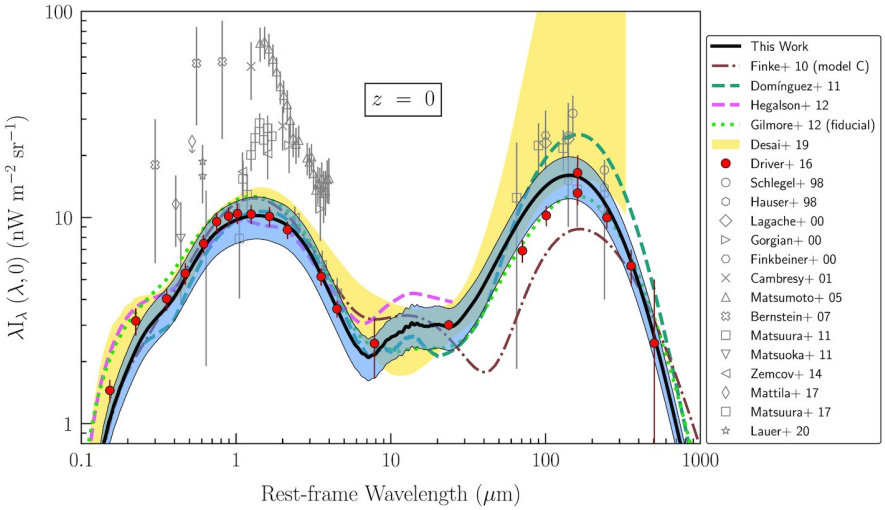


Figure 2.10: The spectral energy distribution of the EBL for $z = 0$ by determined by different models and observation. The black solid line with the blue shaded area show the EBL estimate by Saldana-Lopez et al., 2021 and its $1\sigma$ standard deviation. (Saldana-Lopez et al., 2021)

of the source, l the proper distance and $n_\epsilon$ is the number density of the EBL photons with energy $\epsilon$. $\mu = \cos\theta$, with $\theta$ being the angle between the two photons. $\sigma_{\gamma\gamma}$ is the cross section for the scattering of two photons that depends on the that redshift and on $\beta' = (1 - \epsilon'_{th}/\epsilon)^{1/2}$ and hence on the photons energy.

# Chapter 3

# Particle cascades from gamma-ray bursts

## 3.1 Cascade emission origin

An additional emission from GRBs might come from secondary gamma-rays produced by the line-of-sight-interactions of protons accelerated in the GRB with background radiation fields. A schematic picture of this cascade is shown in figure 3.1. As discussed in the previous chapter, can all protons escaping the gamma-rays burst potentially scatter with background radiation fields, such as the EBL, and produce secondary gamma-rays that can contribute to the observed gamma-ray flux. Therefore the flux of GRBs observed on earth might consists of two contributions. The first is the gamma-ray flux that directly comes from emission processes of the GRB $\frac{dN_\gamma}{dE}$ and is attenuated due to interactions with the EBL. The second contribution $\frac{dN_{casc}}{dE}$, is the flux that comes from the cascade induced by protons escaping the source. In total the observed flux is:

$$\frac{dN_{observed}}{dE} = \frac{dN_\gamma}{dE} \cdot e^{-\tau} + \frac{dN_{casc}}{dE}. \tag{3.1}$$

## 3.2 How cascade emission can explain high-energy emission

What makes the cascade contribution interesting is the possibility that it accounts for very high energy gamma rays observed at energies, at which one would normally not expect any observation, due to EBL attenuation. Primary and secondary gamma-rays have a different scaling with distance $d$ due to the different roles of the EBL. For proton-initiated cascades, they serve as a target for photopion and Bethe-Heitler pair production, leading to the creation of secondary gamma rays, whereas for primary

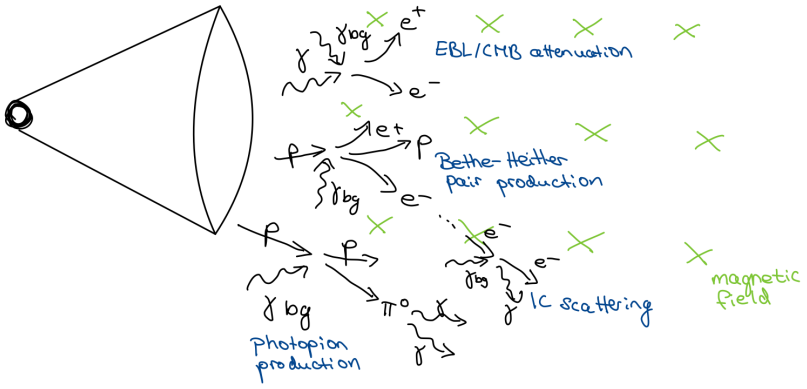


Figure 3.1: The picture shows interactions of primary gamma rays and escaping protons with background radiation fields. The interaction of primary gamma-rays leads to attenuation of the flux, whereas the interaction of escaping protons with background radiation fields leads to cascades that contribute to the observed gamma-ray flux.

gamma rays they lead to pair production, causing exponential attenuation. Therefore the primary gamma-ray flux scales as (Essey et al., 2011 ):

$$F_{primary,\gamma}(d) \propto \frac{1}{d^2} \cdot e^{-\frac{d}{\lambda_\gamma}}, \tag{3.2}$$

whereas the secondary gamma-rays scale with

$$F_{secondary,\gamma}(d) = \frac{p\lambda_\gamma}{4\pi d^2} = \begin{cases} \frac{1}{d} & \text{for } d \gg \lambda_\gamma, \\ \frac{1}{d^2} & \text{for } d \ll \lambda_\gamma \end{cases} \tag{3.3}$$

where $p$ is the rate of protons producing gamma-rays per unit length of the path and $\lambda_\gamma$ is the attenuation length.
An additional feature of the gamma-ray emission of these cascades is that it can arrive at Earth with a time delay. The gamma rays produced in these proton-induced cascades result from charged particles interacting with background radiation fields. These charged particles get deflected in magnetic fields. Hence, the path from the origin of the secondary gamma rays to the observer on Earth is longer than for primary gamma rays, which reach the Earth directly. The more charged particles are deflected away from the line of sight, the greater the time delay of the gamma rays they produce. This also results in more secondary gamma rays reaching Earth with a greater time delay in the case of stronger magnetic fields.
Proton induced cascades are multi-messenger phenomena, because neutrinos can be produced alongside the gamma-rays. Therefore non-detection by observatories such as

IceCube provides an upper limits for the acceleration of protons.

## 3.3 Cascade emission from prompt emission of GRB 221009A

The GRB 221009A is particularly interesting for studying the possibility of cascade emissions, due to it being the first GRB detected with photon energies up to 13 TeV (Cao et al., 2023a). This high energy radiation is hard to be explained solely by leptonic models (Das et al., 2023).
The maximal energy protons are able to gain during their acceleration is important for studying the cascade contribution, because the proton energy determines which scattering processes are possible and contribute to the observed spectra. Rudolph et al. (2023) investigated a multi-messenger model for the prompt emission of GRB 221009A within the internal shock model. They were able to reproduce the observed light curves and were able to produce average proton energies between $1.1 \cdot 10^{21}$ eV - $23.7 \cdot 10^{21}$ eV depending on the average collision radius and whether synchrotron or inverse Compton cooling dominated. Additionally they noted that for the GRB 221009A the LHAASO gamma-ray flux within a time window of 2000 s after the trigger can only be accommodated by ultra-high-energy cosmic ray (UHECR) acceleration within the prompt emission phase due to the introduced time delay by deflection of protons in extragalactic magnetic fields (EGMFs).

# Chapter 4

# Detection of GRBs

The emission of GRBs spans a broad spectrum of electromagnetic radiation, ranging from gamma-rays during the prompt emission to optical emission during the afterglow. In the following chapter we want to focus on the detectors whose data are used in the subsequent chapters, focusing on gamma-ray photon energies. As GRBs are also thought to accelerate cosmic rays, neutrinos from emission processes within the GRB and from line-of-sight interactions of escaping protons are expected. Also until now no detections of neutrinos from GRB are confirmed, the non-detection by current observatories can help to set constraints on the acceleration of cosmic rays.

## 4.1 Gamma-ray detection

The gamma-rays emitted by GRBs can be detected using different techniques. The necessary detection area increases with the energy, because the flux decreases (Funk, 2015). Whereas for lower energies a space based, direct detection is possible, for higher energies a ground based detection, relying on the interaction of the gamma rays with the atmosphere, producing secondary particles is necessary.
Following the review by Funk (2015), there are two different detector types used for ground based detection. The first are imaging atmospheric Cherenkov telescopess (IACTs), that detect the Cherenkov light, produced by gamma-ray induced air showers, in the atmosphere. The detected Cherenkov light is a faint blue light produced by charged particles moving faster than the speed of light in a medium. The second detector type, are water Cherenkov detectors. They detect the Cherenkov light of the charged secondary particles in water tanks. Because these water Cherenkov detectors require the secondary particles to reach the ground, they can only be used for the detection of higher energy gamma rays.

### 4.1.1 HESS

The High Energy Stereoscopic System (HESS), is an IACT and is located in Nambia. It started operating in 2004 with 4 telescopes, but since then several improvements have been made, including a fifth telescope in 2012 (H.E.S.S. collaboration, n.d.). Figure 4.1 shows how IACTs, such as HESS work. The incident gamma ray produces an electron-positron pair in the presence of a nucleus in the atmosphere (Errando et al., 2023). These particles can then create electromagnetic air showers by emitting bremsstrahlung, creating secondary gamma-rays, that can again pair-produce (Errando et al., 2023). These charged electrons and positrons emit Cherenkov radiation, which is detected by the HESS. The Cherenkov light is beamed in the secondary particles' direction and hence can be used to estimate the direction of the initially incoming gamma ray. The HESS can using this technique detect gamma rays in the energy range from tens of GeV to tens of TeV (H.E.S.S. collaboration, n.d.).

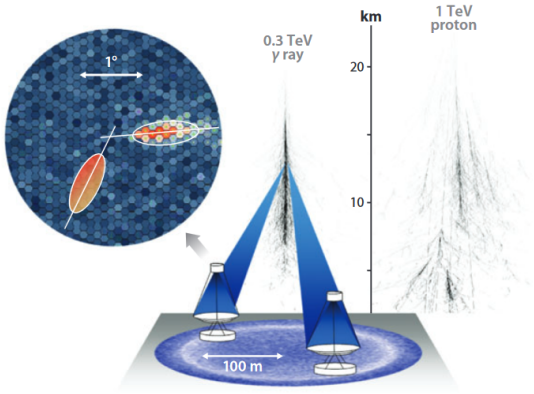


Figure 4.1: The working principle of IACTs and the difference in the shower evolution of gamma ray-induced showers on the left and cosmic ray-induced on the right. (Hinton et al., 2009)

Cosmic ray particles, including protons, can also induce air shows. To differentiate between gamma ray-induced and cosmic ray-induced air showers the difference in the shower development, which can be seen in figure 4.1 is used.

The difference arises because gamma rays and cosmic rays interact differently with the atmosphere. Matthews (2005) describes the evolution of cosmic ray particles induced hadronic air showers the following. In the collision of cosmic rays for example, protons, with air molecules pions are created. Charged pions can then further interact with the atmosphere producing more pions, and eventually decay into muons, that can reach the ground. Neutral pions decay immediately and produce gamma rays that can produce electromagnetic subshowers.

This leads to a difference in the apparent images of the Cherenkow light. Due to neutral pion-induced electromagnetic subshowers, cosmic ray-induced air showers appear more irregular than gamma ray-induced and can be filtered out (Errando et al., 2023).

### 4.1.2 LHAASO

The LHAASO (Large High altitude Air Shower Observatory) is located at an altitude of 4410 m above sea level in China (Zuo et al., 2015). Its schematic structure is shown in figure 4.2. The LHAASO is a hybrid extensive air shower array (Aharonian et al., 2021). That means it detects cosmic rays as well as gamma rays using the air shower they produce when interacting with the atmosphere using different detector types. It consists of a 1.3 $km^2$ array (KM2A), a 78.000 $m^2$ water Cherenkov detector array (WCDA) as well as 18 wide field Cherenkov telescopes (Aharonian et al., 2021). The data from LHAASO used in the following were taken with KM2A and WCDA.

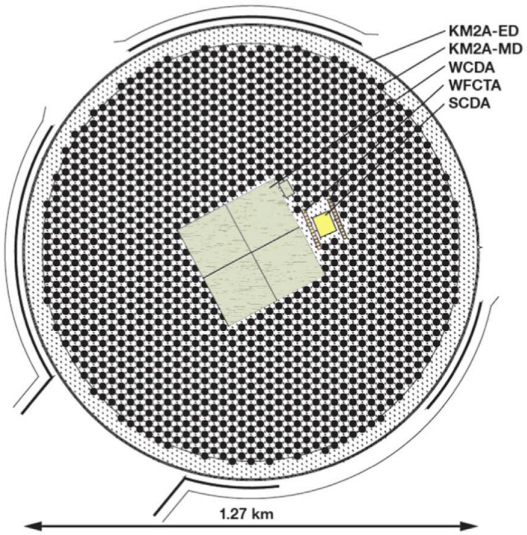


Figure 4.2: The schematic structure of the LHAASO observatory consiting of several detectrs, including the WCDA and KM2A. (Zuo et al., 2015)

The following description of the KM2A detector is based on the paper by Aharonian et al. (2021). The KM2A detector array consists of 5195 electromagnetic detectors and 1188 muon detectors. The electromagnetic detectors are covered with a lead plate that absorbs low-energy particles produced in the air showers and converts gamma rays to electron-positron pairs that excite the beneath-found scintillator medium. The produced scintillation photons are read out using a photomultiplier and therefore the particle numbers and arriving times can be measured. The muon detectors are water-filled concrete tanks. They are covered with 2.5 m of soil so that nearly all particles reaching the detector are muons, whose Cherenkov radiation can be detected using a photomultiplier on top of the tank. Using the charge and time information of the detectors the gamma-ray events can be reconstructed using shower reconstruction algorithms.

To differentiate gamma-ray events from cosmic ray events the ratio between muons and electrons is used, because cosmic ray-induced showers are typically muon-rich whereas gamma-ray showers are muon-poor.

Muons are mainly produced when the charged pions decay. As mentioned in the section before, pions are primary constituents of hadronic cascades, produced by cosmic rays. In electromagnetic showers, the probability of producing a pion through photoproduction processes is very small compared to the production of electron positron

pairs (Fletcher et al., 1994). Hence, the muon content of gamma-ray-induced air showers is way smaller than that of cosmic ray-induced air showers.

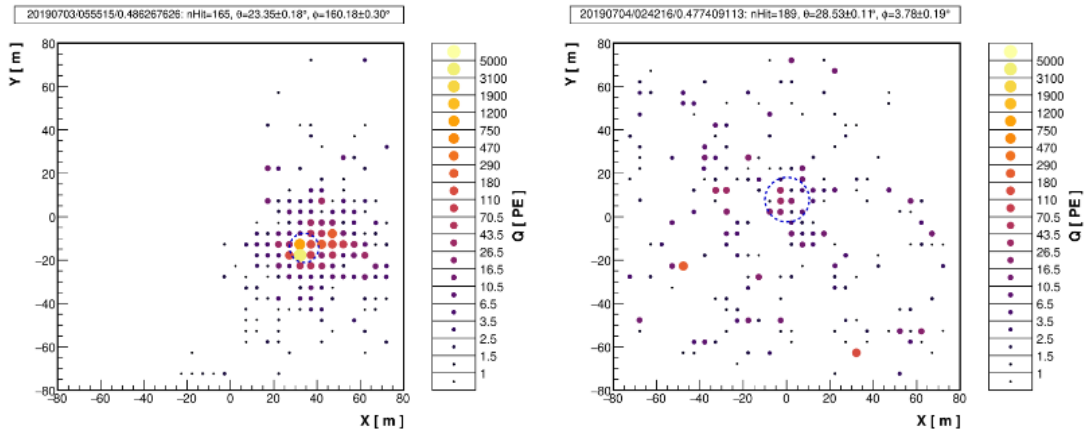


Figure 4.3: The figure shows a high-confidence gamma-ray event, observed by WCDA, on the left, and a cosmic ray background event on the right. (LHAASO collaboration, 2021)

The following description of the WCDA detector is based on the paper by the LHAASO collaboration (2021). The WCDA consists of three independent water Cherenkov detector arrays. In each of them, several photomultipliers are placed on the bottom, separated by non-reflecting plastic curtains. The photomultipliers measure the Cherenkov light produced by secondary particles from the cosmic ray or gamma-ray-induced air showers. They collect data about the particle numbers and arriving times, which can later be used to recalculate the air shower direction, as well as the energy of the primary particle. The separation between cosmic-ray-induced and gamma-ray-induced showers is achieved using their difference in the shower structure. As mentioned before, are cosmic ray-induced showers muon-rich. These muons obtain the transverse momentum of the pion once they decay and can easily reach the ground. Hence, they are widely distributed over the detector area. This makes gamma ray-induced air showers more compact than cosmic ray-induced. Figure 4.3 shows the different detection patterns of a high-confidence gamma-ray event on the left and a high-confidence cosmic ray event on the right.

### 4.1.3 Fermi LAT

The Fermi gamma-ray telescope was launched in 2008 by NASA (Atwood et al., 2009). The main instrument onboard the spacecraft is the Large Area Space Telescope (LAT), which covers an energy range from below 20 MeV to more than 300 GeV (Atwood et al., 2009). A second experiment onboard is the Gamma-Ray Burst Monitor (GBM),

which has an energy range of $\sim 8$ keV to $\sim 40$ MeV (Meegan et al., 2009).

In this section, we want to focus on the Fermi LAT and briefly describe its construction and working principle following the review by Atwood et al. (2009). The Fermi LAT is a pair-conversion telescope, meaning that an incoming gamma ray is converted into an electron-positron pair. It consists of a precision converter-tracker, a calorimeter, an anticoincidence detector, and a trigger and data acquisition system. In the precision converter-tracker, consisting of several layers of high-Z material, the gamma-ray produces an electron-positron pair. Between these layers silicon strip detectors are placed, so that the path of the created particles can be tracked. Around the tracker an anticoincidence detector is placed, so that events produced by charged particles entering the detector are rejected. The energy deposition is measured by several calorimeters, which are located below the tracker. The calorimeters are made from CsI(Tl) crystals and each of them is connected to a photodiode. Figure 4.4 shows this detection principle schematically. Using the different data from the detectors the incident photons' energy and direction can be reconstructed and depending on the accuracy of the energy and position accuracy it is classified into different event classes.

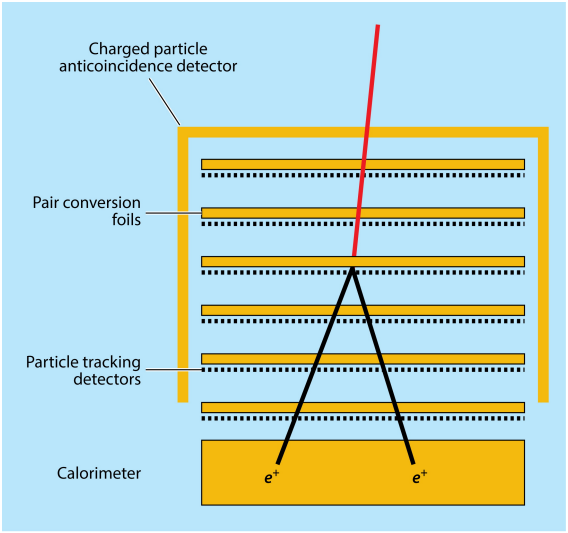


Madejski G. 2016.
Annu. Rev. Astron. Astrophys. 54:725–60

Figure 4.4: The detection principle of the Fermi LAT detector. An incoming gamma ray in red is converted into an electron-positron pair. (Madejski et al., 2016)

## 4.2 Detection of Neutrinos

Neutrinos are neutral-charged elementary particles that only have a very small mass. Hence, these particles can reach Earth without being deflected in magnetic fields and nearly without being absorbed (Halzen et al., 2010). The weak interaction with matter makes big observatories necessary to detect and determine the origin of the incident neutrinos.

### 4.2.1 IceCube

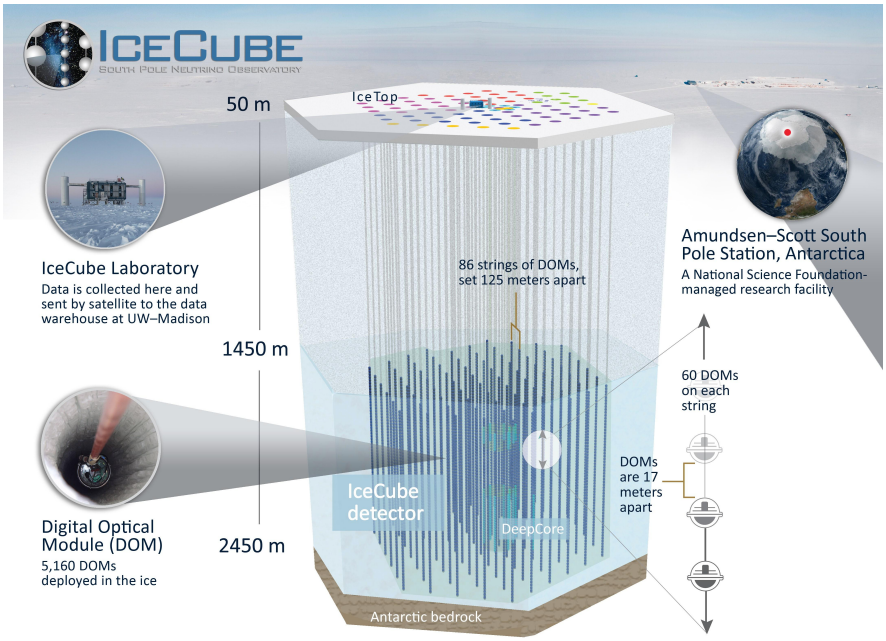


Figure 4.5: The IceCube neutrino detector consisting of 5160 digital optical modules buried in the ice of Antarctica. (IceCube, n.d.)

IceCube is a neutrino observatory located in Antarctica. A schematic description of it is shown in figure 4.5. The following description of the detector and its working principle follows the review by Halzen et al. (2010).
The IceCube observatory was completed in 2011 and consists of 5160 digital optical modules, which are embedded in the Antarctican ice. Each of the digital optical modules has a 25 cm long photomultiplier tube and a data acquisition system. Neutrinos are observed when they interact with the ice molecules via charged and neutral current interactions. Charge-current interactions produce a lepton. These leptons obtain on average 50% of the neutrino's energy for neutrino energies of 10 GeV and up to 80% for high-energy neutrinos. The remaining energy is deposited into the nucleon, inducing a hadronic shower. In neutral current interactions, only a hadronic shower is produced, when the neutrino transfers a fraction of its energy to the nucleon. The produced secondary particles emit Cherenkov radiation. Using the arrival time and amount of Cherenkov radiation observed by the different photomultipliers the incidents neutrinos track and energy is reconstructed using Monte Carlo simulations.

# Chapter 5

# GRB 221009A

## 5.1 Detection of GRB 221009A

GRB 221009A is the brightest GRB ever observed. Its total isotropic-equivalent released energy is determined to be $E_{\gamma,iso} = 1 \cdot 10^{55}$ erg (Lesage et al., 2023). Figure 5.1 shows a comparison between the previous record holders and the reconstructed brightness of GRB 221009A using Fermi data.

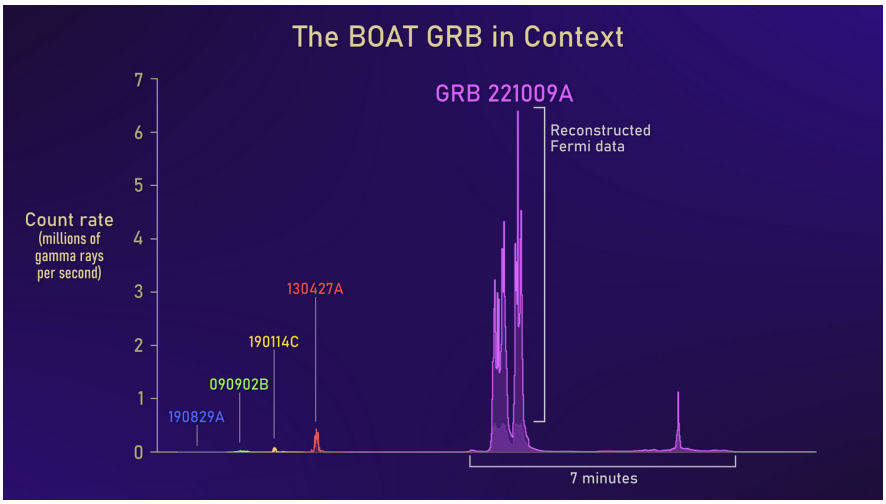


Figure 5.1: Picture taken from (NASA's Goddard Space Flight Center and Adam Goldstein (USRA), n.d.)

GRB221009A was discovered on the 9th October 2022 at 13:16:59.99 Coordinated universal time (UTC) by the Fermi Gamma-Ray Burst Monitor (Veres et al., 2022) About an hour later it was also detected by the Burst Alert Telescope (BAT) on board of the Swift satellite. Additionally the X-ray telescope (XRT) and Ultra Violet and Optical Telescope (UVOT) onboard of Swift observed it, yielding a position of $RA_{J2000} = 288.26452, DEC_{J2000} = 19.77350$ with a 90%-confidence error radius of about 0.61 arc seconds (Dichiara et al., 2022). Observations of the absorption lines

found in the afterglow emission by the Very Large Telescope (VLT) determined a redshift of $z = 0.151$ for the GRB (de Ugarte Postigo et al., 2022). Furthermore the non-detection of neutrinos by IceCube between 200 s before the trigger and 2000 s after (Abbasi et al., 2023) sets strong constraints on the acceleration of UHECR.

### 5.1.1 The LHAASO data

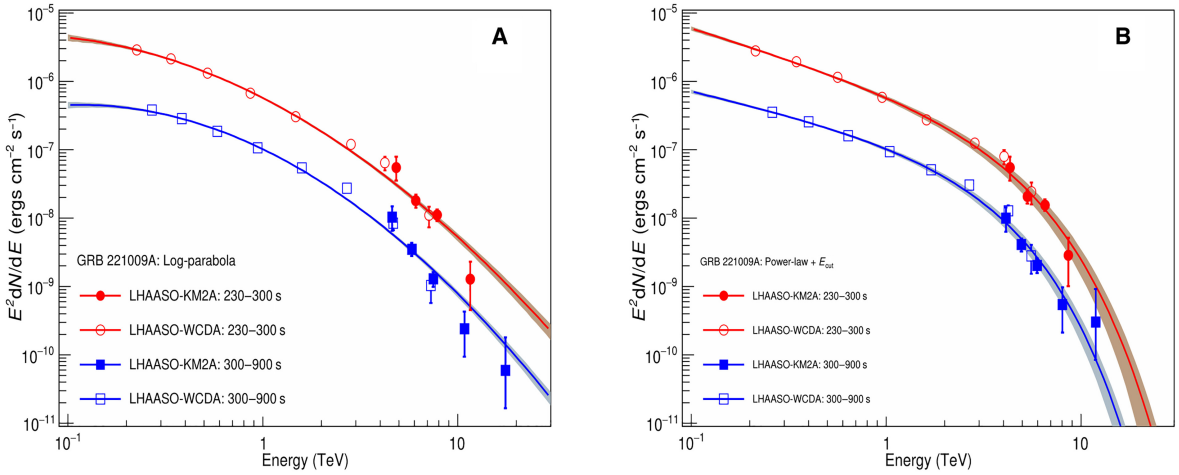


Figure 5.2: The observed spectra of GRB 221009A by LHAASO. The unfilled points are the WCDA data points and the filled the KM2A data points. In picture A a log-parabola function is used to fit the observational data whereas in figure B power-law with exponential cutoff function is used to fit the observational data. (Cao et al., 2023a)

The GRB was additionally observed by the KM2A and WCDA experiments at the LHAASO observatory. LHAASO detected gamma-rays at very high energies up to 13 TeV making GRB 221009A the first GRB ever recorded at this high gamma-ray energies (Cao et al., 2023b). During the first 3000 seconds after the trigger by GBM more than 64,000 photons with energies above 0.2 TeV were detected (Cao et al., 2023b). Additionally between 230 s − 900 s after the GRB eight events with energies above 10 TeV were reconstructed (Cao et al., 2023b).
Figure 5.2 shows the observed spectra of the GRB 221009A by LHAASO. The flux observed with KM2A at the median energy, assuming a power-law with exponetial cutoff, can be seen as data point in plot B of figure 5.2. These values are later used as data points to restrict the cascade contribution.
The individual WCDA data points shown in figure 5.2 are not publicly available. However, the best-fit parameters of a power-law fit to the WCDA flux points, assuming the Saldana-Lopez et al. (2021) EBL model, are provided in table S2 of Cao et al. (2023b). The obtained prefactor of $(21.77 \pm 0.47) \cdot 10^{-8}$ TeV$^{-1}$ cm$^{-2}$ s$^{-1}$ and the spectral index

$\Gamma = 2.231 \pm 0.026$ are later used to set a prior on the primary gamma-ray emission from GRB 221009A.

### 5.1.2 The HESS data

HESS started the observation of GRB 221009A on the third night after the GRB. Due to poor atmospheric condition only data from nights 3, 4 and 9 are available (Aharonian et al., 2023b). They did not find any significant emission from the source and derived an upper limit, asumming a power-law with spectral index of 2 as source spectrum. These upper limits on the flux, during the third night and averaged over the full observation period are shown in figure 5.3. The averaged flux over all nights, which can be found in the auxiliary material on the website of the H.E.S.S. Collaboration (n.d.) are later used for comparing the cascade predicted flux with the late-time observations.

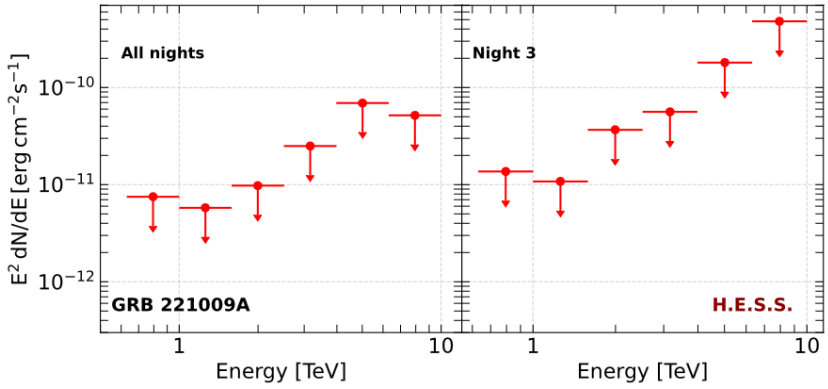


Figure 5.3: Derived upper flux limits for HESS. The left side shows the upper flux limit for the third night after the GRB and the right side the upper flux limit for the full observation period of night 3 to night 9 after the GRB. (Aharonian et al., 2023b)

### 5.1.3 Fermi LAT data

Fermi LAT detected the first high-energy emission from GRB 221009A at 14:17:05.99 on October, 09 2022 (Bissaldi et al., 2022). Due to its extreme brightness the instrument suffered from severe pile-up effects during the main emission periods in the time intervals of 225 to 236 seconds and 257 to 265 seconds after the GBM trigger (Omodei et al., 2022).
Due to this issue we focused on the analysis of the Fermi LAT data during the HESS observation period, which gives the opportunity to study the possible emission from proton-induced cascades during later observation times.

### Analysing the Fermi LAT data

Fermi LAT is constantly monitoring the gamma- ray sky. The first step in the analysis therefore is to select the data associated with the GRB. The spacecraft and event files necessary for the analysis can be downloaded from the website of the Fermi spacecraft (NASA, n.d.(b)). An event file includes all data from the photons detected by Fermi LAT, including the energy, and the reconstructed origins of the gamma-rays. The spacecraft-file includes all parameters of the spacecraft, for example its position and its inclination. To download the data the gamma-ray burst position (RA: 288.266, DEC: 19.773), the energy range (100 MeV - 1 TeV), and the search radius (20°) need to be selected, as well as the observation period.
The analysis of the data itself is performed using the fermipy python package (Wood et al., 2017). The selection criteria, used in the configuration file, follow the LAT data selection recommendations (NASA, n.d.(a)). The event class selected is 128, the event type is front-back, and the `P8R3_SOURCE_V3` response function is used for the analysis. Additionally, a maximum zenith angle of 90° is applied, to filter out photons originating from the Earth's upper atmosphere. Furthermore, a model for the galactic and isotropic background according to the chosen event type are selected.

**Modelling the background** The GRB is only one of many sources in the region of interest (ROI). This makes it necessary to model the different sources in the background to calculate the photon flux from the GRB. For this the fermipy packages uses a binned likelihood analysis, where the likelihood is the probability to obtain the observed data under an assumed model (NASA, 2018).
For modelling the background a two year period of the $10° \times 10°$ region around the later position of the GRB, (RA: 288.21, DEC: 19.73) is analysed. The GRB is positioned behind the galactic plane, which becomes already clear looking at the gamma-ray bursts position in galactic coordinates: galactic longitude 52.98 (deg) and galactic latitude 4.34 (deg). These makes the background as well as the gamma-ray burst hard to model. Figure 5.4 shows the number of gamma-rays detected during the two years before the gamma-ray burst, where in the lower left corner the emission from the Milky Way can be seen.

In the analysis the spectral and norm parameter of all sources within a 5° degree region of the center and a ts value above 4 and more than 1 predicted photon are left free to vary. Additionally the norm parameter for all sources within a 10° degree region, a ts value above 4 and more than 1 predicted photon are left free. Furthermore, the norm parameter of the galactic diffusive background and all parameters of the isotropic background are left free to vary. The figure 5.5 shows the residual map calculated using the fermipy package. The central region around the later position of the GRB shows a

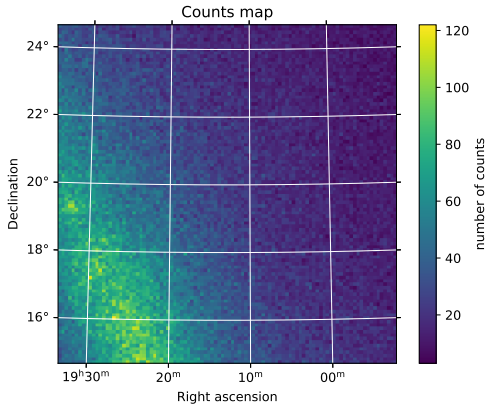


Figure 5.4: Counts map showing the number of counts per special bin during the two year long observations before the GRB.

small deviation from the model, whereas larger deviation from the obtained model are found in modelling the Milky Way. Figure 5.6 shows additionally the PS map (Bruel, 2021), that also takes the energy dependent point spread function (PSF) into account when calculating the residuals.

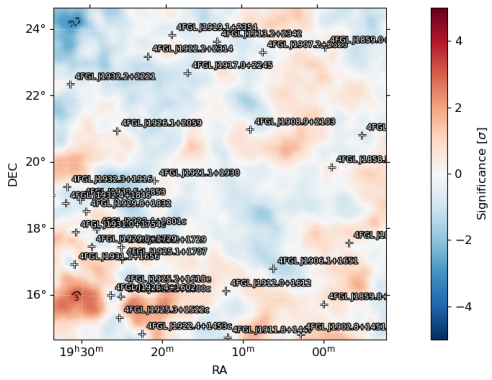


Figure 5.5: Residual map showing the difference between the obtained model of the ROI and the two year long observations before the GRB.

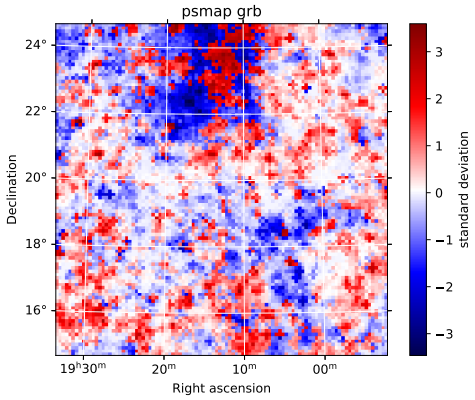


Figure 5.6: PS residual map showing the difference between the final obtained model of the ROI and the raw two year observational data before the GRB.

**Modelling the GRB** The model, derived from two years of observational data centered on the position of the later GRB, is used as the background model for the analysis of GRB 221009A. Also here a $10° \times 10°$ region is analysed and only the norm parameters of sources within $1°$ and are left free to vary, whereas all other are fixed to the values obtained during the background analysis. The GRB itself is added as point source with power law spectral function at the position of a right ascension of

288.21 and a declination of 19.73. We choose an observation period starting with the observation of HESS at $t_0 + 1.901 \cdot 10^5$ s, where $t_0$ is the triggering time of Fermi GMB, and the end of the HESS observation period at $t_0 + 7.122 \cdot 10^5$ s. Figure 5.7 shows the residual map calculated by fermipy and figure 5.8 the PS map. Both show sometimes even more than $2\sigma$ discrepancy, which probably also is caused by the very short observation times.

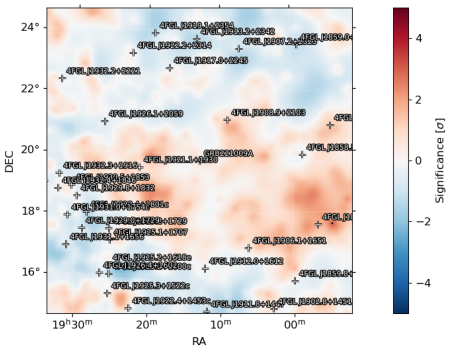


Figure 5.7: Residual map showing the difference between the obtained model of the ROI and the observational data from $t_0 + 1.901 \cdot 10^5$ s, where $t_0$ is the triggering time of Fermi GMB, and the end of the HESS observation period at $t_0 + 7.122 \cdot 10^5$ s.

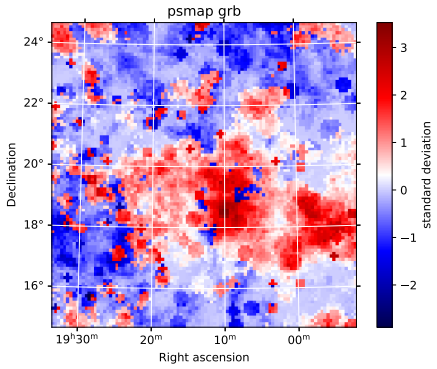


Figure 5.8: PS residual map showing the difference between the final obtained model of the ROI and the raw observational data from $t_0$+1.901·$10^5$ s, where $t_0$ is the triggering time of Fermi GMB, and the end of the HESS observation period at $t_0 + 7.122 \cdot 10^5$ s.

Figure 5.9 shows the spectral energy distribution (SED) obtained for GRB 221009A, assuming a point source with power law spectrum. It can be seen that no significant flux was observed by Fermi LAT during this late time observation of the GRB. Accordingly only an upper flux limit could be determined.

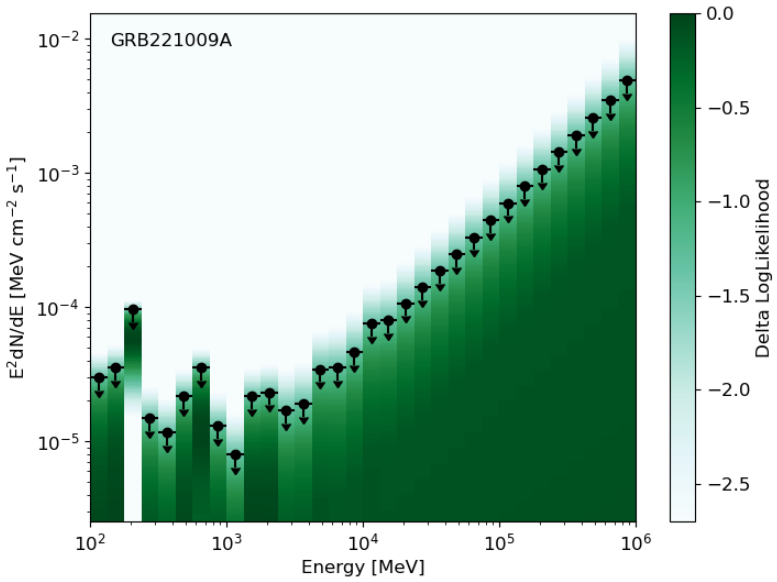


Figure 5.9: SED obtained for GRB 221009 for the time interval of $1.901 \cdot 10^5$ s until $7.122 \cdot 10^5$ s after the trigger by Fermi GBM.

# Chapter 6

# Constraining the cascade contribution of GRB 221009A

After discussing the theoretical model of GRBs and the peculiarities of GRB 221009A, I will continue with my work on the simulation of proton-induced cascades and discuss their possible contribution to neutrino flux and their contribution to the observed flux at gamma-ray energies.

## 6.1 Simulating cascades using CRPropa

For modeling the gamma-ray and the neutrino spectrum generated by proton-induced cascades, the simCRpropa[1] simulation code, which is based on the CRPropa Monte Carlo simulation package version 3.1.6 Alves Batista et al. (2022), is used. CRPropa is a numerical simulation framework that makes it possible to study the propagation of ultra-high energy particles through the universe. The program has all aspects of the particle propagation, from the calculation of the propagation to the scattering in separate modules, over which the simulation loops over. Therefore there are different propagation and interaction modules available that can be added to a simulation. A full list of the available modules can be found at CRPropa Developers (n.d.)
To simulate the cascade of a GRB a source is placed in the center of an observer sphere, which has a radius equal to the co-moving distance $D$ of the source. From the source particles, in our case protons, are injected uniformly in a cone of a given opening angle $\theta$. The particles propagate from the source outwards and as they reach the observer sphere, their momentum, energy, and position are saved in an output file. The time delay of a particle is calculated by (Aharonian et al., 2023a):

$$\tau \approx \frac{d - D}{c}, \tag{6.1}$$

[1] `https://github.com/me-manu/simCRpropa`

where $d$ is the particle's propagation length and $c$ is the speed of light. Because the observer is only a very small point on the observation sphere, a parallel transformation is used to reduce the number of necessary simulations (Alves Batista et al., 2016).
The simulation itself tracks the particle's motion in cell-like period boxes, with a randomly oriented magnetic field of a chosen strength. During its propagation, the program uses Monte Carlo methods to determine whether the particle interacts with background radiation fields. It takes all relevant interactions and energy loss processes into account, namely synchrotron emission, IC scattering, pair-production, photopoion production, photodisintegration, nuclear decay, and adiabatic losses due to the expansion of the Universe and includes the CMB, EBL and ultraviolet background radiation as target photon fields.
An important parameter of the simulation is its time resolution. LHAASO observed the high energy gamma rays within a 2000s time window after the GRB. This short time window is hard to model using CRPropa, due to numerical inaccuracies. Figure 6.1 shows the time delay of the detected photons for a simulation with a minimal time resolution of 2 minutes and an assumed magnetic field strength of $B = 1 \cdot 10^{-20}$ G, binned into 200 s time bins. In this figure, several properties that led us to increase the minimal time resolution to 6000 s can be seen. The first feature is that one can see that some photons have a negative time delay. This is physically impossible and hence comes from numerical errors. The second is a double hump structure at small time delays, with one around a time delay of 1800 s and the other around 4000 s. Therefore we decided to use a minimal time delay of 6000 s and analyse only this first time bin together because the time delay within the first 6000 s seems to be largely influenced by numerical errors.

Nevertheless, a time resolution of 6000 s is still very small, resulting in large computation times. To reduce the runtime we apply maximal thinning by setting the thinning parameter $\eta$, which determines whether a secondary particle is tracked, to 1. Using the output of the simulation, a histogram of the number of counts per injected energy $\epsilon$, observed energy $E$, solid angle $d\Omega$, time delay $\tau$, and energy interval of the injected particle $\Delta\epsilon$ can be obtained (Aharonian et al., 2023a):

$$\frac{dN}{d\epsilon dE d\Omega} = \frac{1}{N_{inj}(\Delta\epsilon)} \frac{N}{\Delta\epsilon \Delta E \Delta\tau \Delta\Omega}. \tag{6.2}$$

To obtain the time-averaged flux at a given energy assuming a certain injection spectrum the gamma-ray or neutrino spectrum needs to be reweighed. This is calculated by (Aharonian et al., 2023a):

$$\frac{dN}{dE d\Omega} = \int_0^\infty d\epsilon \int_0^\infty d\epsilon' \frac{dN}{d\epsilon'} \int_0^{\tau_{max}} d\tau \frac{dN}{d\epsilon' dE d\Omega d\tau} \tag{6.3}$$

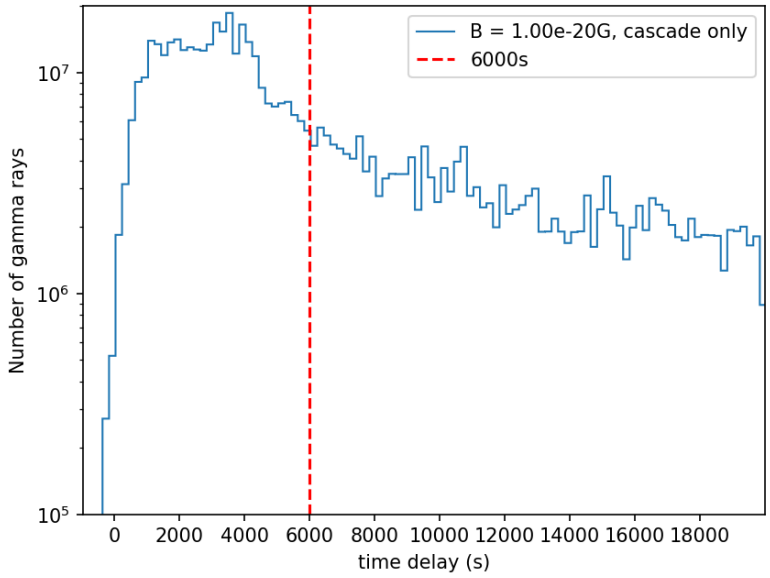


Figure 6.1: Time delay of the photons detected for 40 simulation with $B = 1 \cdot 10^{-20}$G and 10 particles injected in every energy bin.

After all those steps the secondary gamma-ray or neutrino spectrum is obtained, which can then be compared to observational data.

## 6.2 Comparing with LHAASO data

The flux observed during the LHAASO observation window $\frac{dN_{obs}}{dE}$ consists of a contribution from primary gamma-rays $\frac{dN_\gamma}{dE}$ produced directly by the GRB, and a contribution from the cascade $\frac{dN_{cacs}}{dE}$:

$$\frac{dN_{obs}}{dE} = \frac{dN_\gamma}{dE} \cdot e^{-\tau} + \frac{dN_{cacs}}{dE}, \tag{6.4}$$

where $e^{-\tau}$ describes the EBL absorption. The goal is to model the right-hand side of the equation and compare it to the observed flux by LHAASO, on the left side of the equation.

For the primary gamma-ray spectrum a power law of the form

$$\frac{dN_\gamma}{dE} = A \cdot E^{-\Gamma} \tag{6.5}$$

is assumed, where $A$ is the prefactor and $\Gamma$ the spectral index.

The cascade is modeled using simCRpropa. The protons are initially injected in a cone with opening angle $\theta = 1.6°$, consistent with the derived jet opening angle from the jet break observed by Cao et al. (2023b). The protons injection energy ranges from

$10^{12}$ eV to $10^{18}$ eV, and is binned into 24 energy bins. The chosen proton energies lay below the GZK cutoff, which would for higher injection energies strongly increase the necessary simulation time. The chosen proton injection energies are additionally lower than the average maximal proton energy derived by Rudolph et al. (2023). In their simulations of the prompt emission of GRB 221009A, they obtained an average maximal proton energy between $1.1 \cdot 10^{21}$ eV $- 23.7 \cdot 10^{21}$ eV. The assumed injected proton spectrum is given by:

$$\frac{dN}{dE} = A_p \cdot \left(\frac{E}{1 \cdot 10^{12} eV}\right)^{\Gamma_p} \cdot e^{\frac{-E}{E_{cut}}} \cdot e^{\frac{-E_{cut\_low}}{E}}, \tag{6.6}$$

where $A_p$ is the prefactor of the proton spectrum, $\Gamma_p$ is the proton index, $E_{cut}$ is the high energy cut-off and $E_{cut\_low}$ is the low energy cut-off.
Additionally a magnetic field strength of $B = 10^{-18}$ G and $B = 10^{-20}$ G are simulated. In total 500 simulations are performed, where in each simulation 40 protons are injected. In the simulations standard ΛCDM cosmology with $H = 70 \frac{\text{km}}{\text{s Mpc}}$ and $\Omega_m = 0.3$ are assumed. Additionally a time resolution of 6000 s, together with a numerical precision of $1 \cdot 10^{-16}$ are used. The maximum distance a particle is traced is set to 4 Gpc and the minimal energy until which particles are tracked is set to 1 GeV. Additionally, a minimum rigidity of $R = 50$ EeV is used for taking the particle's deflection in magnetic fields into account. The rigidity is defined by $R = \frac{E}{Z}$, where $E$ is the energy in EeV and $Z$ the particle's charge. As observational data to compare the model to, the differential flux measured by KM2A during the time interval of $300 - 900$ s after the GRB is used. The data points were obtained assuming a power law with exponential cut-off and are taken from table S1 in Cao et al. (2023a). To obtain the best fitting values of the modeled primary and cascade spectrum a modified $\chi^2$ loss function for a data point at an energy E is assumed:

$$\chi^2(E) = \begin{cases} \left(\frac{\frac{dN_{KM2A}}{dE}(E) - \frac{dN_{model}}{dE}(E)}{err_n(E)}\right)^2 & \text{if } \frac{dN_{model}}{dE}(E) < \frac{dN_{KM2A}}{dE}(E) \\ \left(\frac{\frac{dN_{KM2A}}{dE}(E) - \frac{dN_{model}}{dE}(E)}{err_p(E)}\right)^2 & \text{if } \frac{dN_{model}}{dE}(E) > \frac{dN_{KM2A}}{dE}(E) \end{cases} \tag{6.7}$$

where $\frac{dN_{km2a}}{dE}(E)$ is the KM2A flux points central value and $err_p(E)$ and $err_n(E)$ the according upper and lower error bar at a given energy $E$. $\frac{dN_{model}}{dE}(E)$ is the modeled composite flux, consisting of the primary and cascade flux at the energy $E$.
In addition to the KM2A data, the WCDA data are used to constrain the cascade and primary spectrum. Although the individual WCDA data points are not publicly available, the parameters of a power law fit of the intrinsic spectrum for the time interval of $326 - 900$ s assuming Saldana-Lopez et al. (2021) EBL model are available

in table S2 in Cao et al. (2023b). These fit parameters are used to impose a prior on the primary gamma-ray spectrum. The prior on the spectral index of the primary gamma-ray spectrum is given by

$$\text{prior}_\Gamma = \left(\frac{\Gamma - 2.231}{0.026}\right)^2, \tag{6.8}$$

and the prior on the prefactor of the primary spectrum is given by

$$\text{prior}_\text{A} = \left(\frac{\text{A}\left[\frac{1}{\text{TeV s cm}^2}\right] - 21.77 \cdot 10^{-8}\ \frac{1}{\text{TeV s cm}^2}}{0.47 \cdot 10^{-8}\ \frac{1}{\text{TeV s cm}^2}}\right)^2. \tag{6.9}$$

The loss function consequently depends on the proton spectrum parameter $A_p$ , $\Gamma_p$, $E_{cut}$ and $E_{cut\_low}$, as well as on the parameters of the primary spectrum $A$, $\Gamma$ and is the sum of all individual $\chi^2$ at every data point plus the sum of the priors:

$$\chi^2_{tot} = \sum_{E=E_{min,KM2A}}^{E=E_{max,KM2A}} \chi^2(E) + \text{prior}_\Gamma + \text{prior}_\text{A}. \tag{6.10}$$

This loss function can be used to find the best model, for example by minimizing it using the python package iminuit (Dembinski et al., 2020). Assuming that the obtained value of the loss function still follows $\chi^2$ statistics, it can be used to determine the goodness of fit, where the lowest value corresponds to the best fit.

### 6.2.1 Determining a limit for the cascade contribution

Figure 6.2 shows the observed and intrinsic spectrum of the WCDA and the KM2A data. The observed spectrum is described by a power law with exponential cut-off, whereas the intrinsic spectrum is described by a power law. In the fitting, the intrinsic spectrum is used as prior to the primary gamma-ray spectrum. To obtain the observed flux this intrinsic power-law needs to be multiplied by the EBL absorption.
This intrinsic spectrum of WCDA multiplied by the EBL absorption already lies within the confidence interval of the first KM2A data point and very close to the last KM2A data point. Therefore the primary gamma ray spectrum without a cascade contribution already describes the data very well. Hence, the best fit function including the cascade is not substantially better than other fit parameters. Therefore, instead of calculating the best fit parameters we want to focus on which parameters for the cascade can be ruled out.

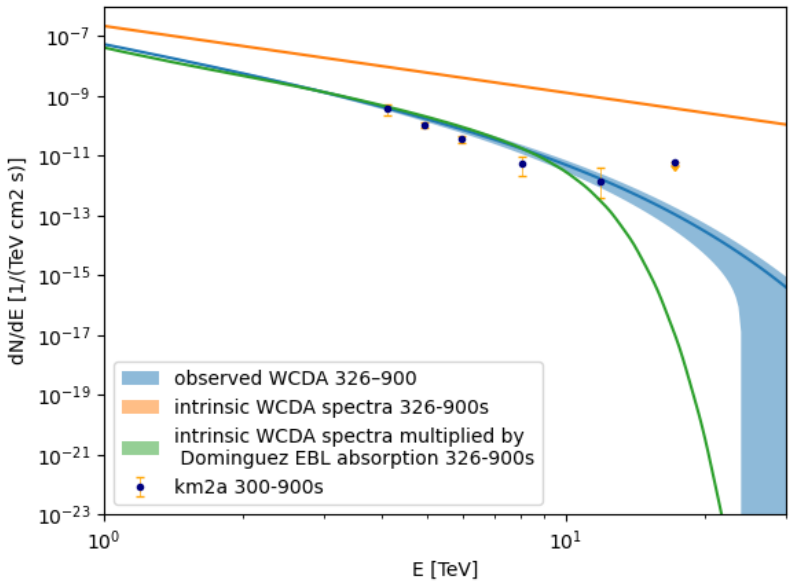


Figure 6.2: WCDA spectral function and KM2A data

**Leaving the cascade parameters free** The first idea is to rule out certain proton spectrum prefactor $A_p$ by keeping the low energy cut-off $E_{cut\_low}$ fixed, but leaving all other parameters free. To ensure that the proton spectrum prefactor lies at a reasonable value, I introduce a scaling factor, so that $A_P = a_p \cdot 10^{-19}\ \frac{\text{protons}}{\text{eV cm}^2\ \text{s}^1}$. Looping over the protons spectrum prefactor $a_p = [0, 1 \cdot 10^{-3}, 1, 10, 100, 1000]$ makes it possible to obtain the $\chi^2$ values for all $a_p$ values. The best fit parameters for the different prefactors $a_p$ can be found in the Appendix A.1.
The obtained $\chi^2$ value rounded to two decimal places is for the different prefactors $a_p$ equal to 46.6 and therefore shows no significant variation for the different $a_p$ values. The obtained parameters, show the tendency, that higher $a_p$ values can be accommodated by changing the cascade parameters, especially by increasing the $\Gamma_p$ value and by changing the high energy cut-off.

**Fixing the cascade parameters** The low and high energy cut-offs are not physical parameters, instead, they account for the minimal and maximal injection energy of the protons. For that reason we decide to fix all cascade parameters, leaving only the primary spectrum parameters free and looping over the proton spectrum prefactor. Also here a scaling factor for the proton spectrum prefactor is used, so that $A_P = a_p \cdot 10^{-19}\ \frac{\text{protons}}{\text{eV cm}^2\ \text{s}^1}$. The low energy cut-off $E_{cut\_low}$ is set to $1 \cdot 10^{12}$ eV, the minimal energy of the injected protons and the high energy cut-off $E_{cut}$ to $1 \cdot 10^{18}$ eV, the maximal energy of the injected protons. Doing this for three values of $\Gamma_p = [2.0, 2.3, 2.7]$, the protons spectrum prefactor $a_p$ can be constrained.

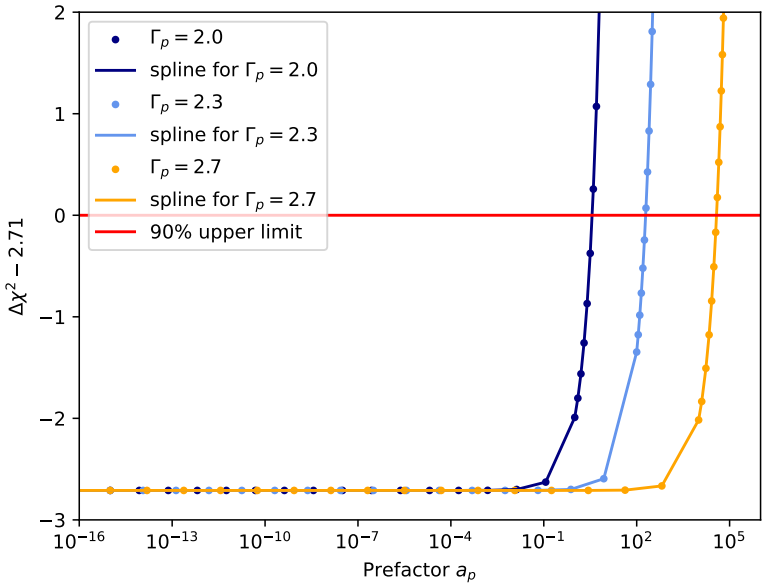


Figure 6.3: The figure shows the obtained $\Delta\chi^2$ values for different assumed proton spectrum prefactors $a_p$, for a magnetic field strength of $10^{-20}$ G

Figure 6.3 shows the obtained $\Delta\chi^2$ values for different proton spectrum prefactors $a_p$, for a magnetic field strength of $10^{-20}$ G. The plot shows that the $\Delta\chi^2$ shows no significant increase for a wide range of parameters. Hence, this range of prefactors, before the $\Delta\chi^2$ value rapidly increases, describes the data similarly well. The 90% upper limit for the prefactor $a_p$ is the value for which $\Delta\chi^2 - 2.71 = 0$.

For $\Gamma_p = 2.0$ the 90% upper limit is $a_p^{90\%} \approx 3.65$. The obtained best-fit spectrum for this prefactor is shown in figure 6.4. The black line shows the the combined spectrum after adding together the primary and cascade contributions. It also shows the separate contributions from the primary gamma-ray emission in orange and the cascade contribution in red. The plot shows that for lower energies the primary spectrum contribution dominates the flux, whereas for energies above 13 TeV the cascade dominates the flux.
For $\Gamma_p = 2.3$ the 90% upper limit for the proton spectrum prefactor is given by $a_p^{90\%} \approx 194.67$ and for $\Gamma_p = 2.7$ the 90% upper limit is $a_p^{90\%} \approx 37849.62$.

Figure 6.5 shows the obtained $\Delta\chi^2$ values for different proton spectrum prefactors $a_p$, for a magnetic field strength of $10^{-18}$ G. One can see that also here a broad range of prefactors describe the data similar good before the $\Delta\chi^2$ value increases. For $\Gamma_p = 2.0$ the 90% upper limit is $a_p^{90\%} \approx 3.57$. Figure 6.6 shows the best-fit spectrum obtained for the 90% upper limit proton prefactor $a_p^{90\%} \approx 3.57$. The solid black line shows the the combined spectrum after adding together the primary and cascade gamma-ray

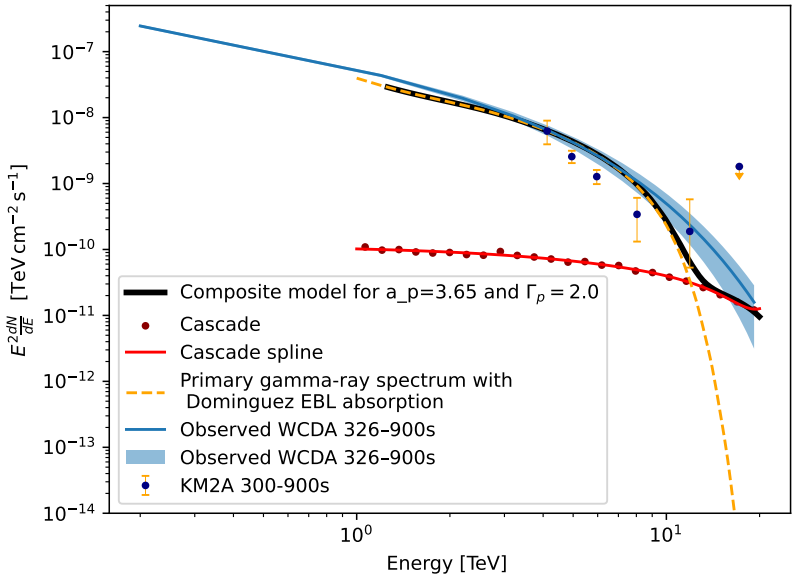


Figure 6.4: The obtained gamma-ray spectrum for the 90% upper limit of the proton spectrum with spectral index of 2.0. It is plotted for the upper limit prefactor $a_p^{90\%} \approx 3.65$, $E_{cut} = 1 \cdot 10^{18}$ eV, $E_{cut\_low} = 1 \cdot 10^{12}$ eV, $A = 210 \cdot 10^{-9}$ $\frac{1}{\text{TeV cm}^2\text{ s}}$, $\Gamma = 2.313$, assuming a magnetic field strength of $10^{-20}$ G.

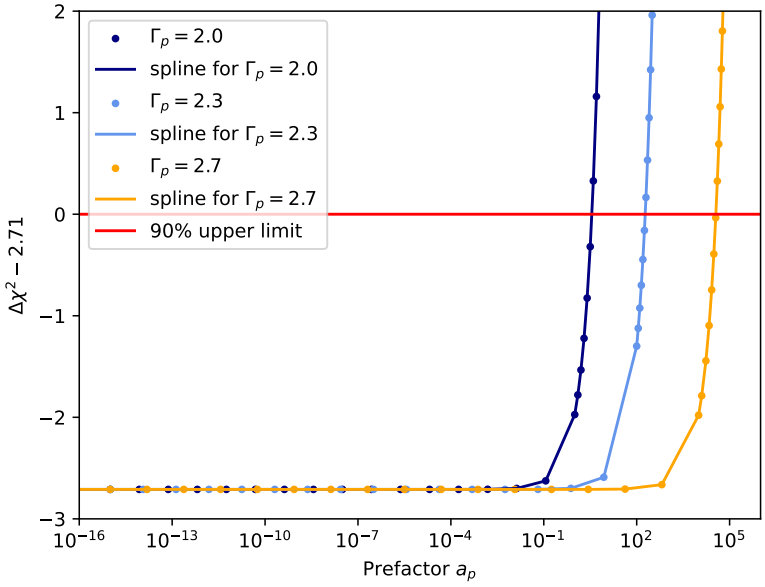


Figure 6.5: The figure shows the obtained $\Delta\chi^2$ values for different assumed proton spectrum prefactors $a_p$ and spectral indices $\Gamma_p$, assuming a magnetic field strength of $10^{-18}$G.

contributions. It also shows the separate contributions from the primary gamma-ray emission in orange and the cascade contribution in red. Also here the primary spectrum contribution dominates for low energies, whereas for energies above 13 TeV the cascade dominates the flux. For $\Gamma_p = 2.3$ the 90% upper limit for the proton spectrum prefactor is given by $a_p^{90\%} \approx 188.5$ and for $\Gamma_p = 2.7$ the 90% upper limit is $a_p^{90\%} \approx 36033.96$. Their best fit spectrum can be found in the Appendix A.1.

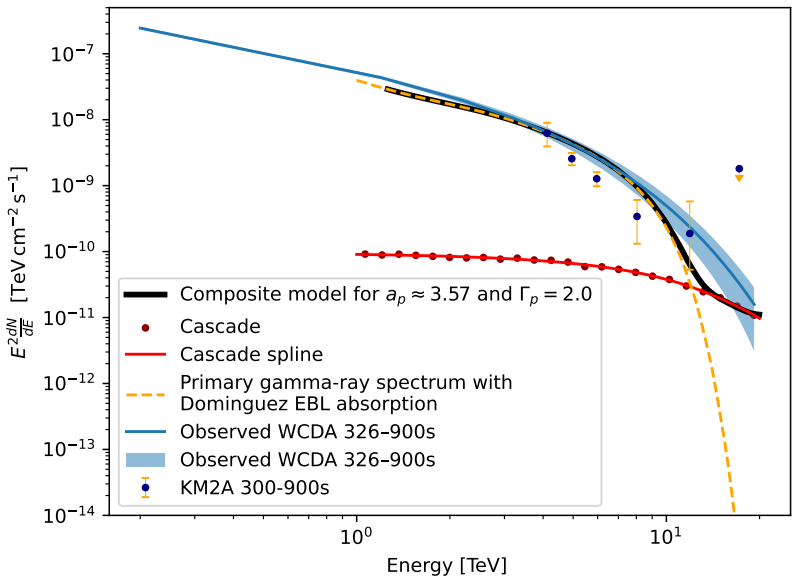


Figure 6.6: The obtained gamma-ray spectrum for the 90% upper limit of the proton spectrum with spectral index of 2.0. It is plotted with the upper limit prefactor $a_p^{90\%} \approx 3.57$, $E_{cut} = 1 \cdot 10^{18}$ eV, $E_{cut\_low} = 1 \cdot 10^{12}$ eV, $A = 210 \cdot 10^{-9} \frac{1}{\text{TeV cm}^2\text{ s}}$, $\Gamma = 2.313$, assuming a magnetic field strength of $10^{-18}$ G.

## 6.3 Comparing with limits from IceCube

If protons escape the GRB they can produce neutrinos through photopion processes. Using CRPropa, the emission of these neutrinos can be simulated and compared to the neutrino upper flux limit obtained from the non-observation of neutrinos from GRB 221009A by IceCube. Because the IceCube detector is mostly sensitive to muon neutrinos, the flux of muon neutrinos observed at earth is calculated.

For the neutrino simulations, the same simulation parameters as for the gamma-ray simulations are used. CRPropa does not take neutrino oscillations into account. The conversion probability is an oscillating function of the distance, but for long distances, such as it is the case for the GRB the oscillation probability behaves randomly. Therefore neutrinos arriving at earth are approximately equally distributed in all three flavors. The simulations using CRPropa give a flavor ratio distribution of electron neu-

trinos to muon neutrinos to tau neutrinos $\nu_e$:$\nu_\mu$:$\nu_\tau$ of 1:2:0. Thus, to obtain the flux of muon neutrinos at earth the muon neutrino flux obtained by the simulation needs to be multiplied by 0.5 to account for the neutrino oscillations.
In figure 6.7 the neutrino upper flux limit obtained by IceCube is shown together with the obtained neutrino spectra for an assumed magnetic field strength of $10^{-20}$ G and different spectral indices of the proton spectrum are shown. The parameters used for the proton spectrum, are the same values previously determined when calculating the upper limit of the proton spectrum prefactor. Figure 6.8 additionally shows the neutrino upper flux limit obtained by IceCube together with the obtained neutrino spectra for an assumed magnetic field strength of $10^{-18}$ G. Also here the parameters used for the proton spectrum, are the same values previously determined when calculating the upper limit of the proton spectrum prefactor.
In both figures the upper limit of the neutrino flux from IceCube lies several orders of magnitude higher than the flux expected from the proton-induced cascades upper limits. Hence, the cascade emissions are consistent with the IceCube upper limits.

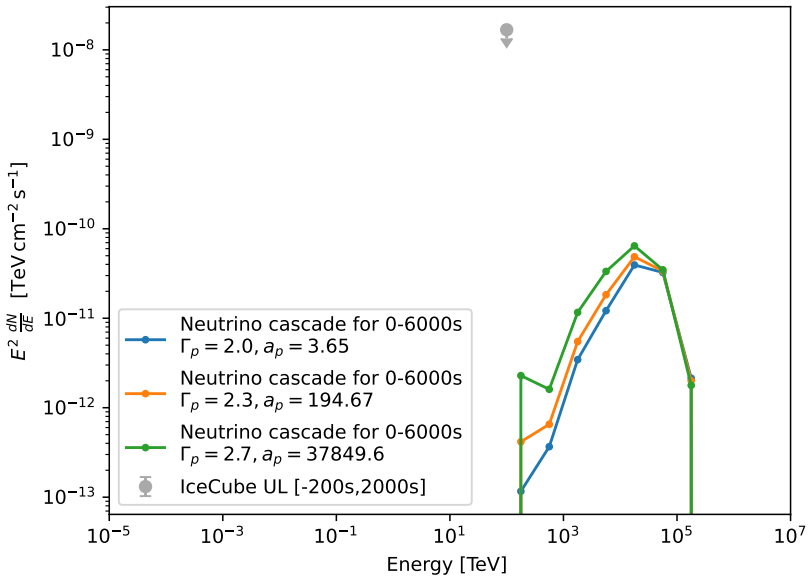


Figure 6.7: The plot shows the IceCube upper limit together with the obtained neutrino spectrum for the different 90% upper limit proton spectrum prefactors, assuming a magnetic field strength of $10^{-20}$ G. The high energy cut-off is set to $E_{cut} = 1 \cdot 10^{18}$ eV and the low energy cut-off to $E_{cut\_low} = 1 \cdot 10^{12}$ eV.

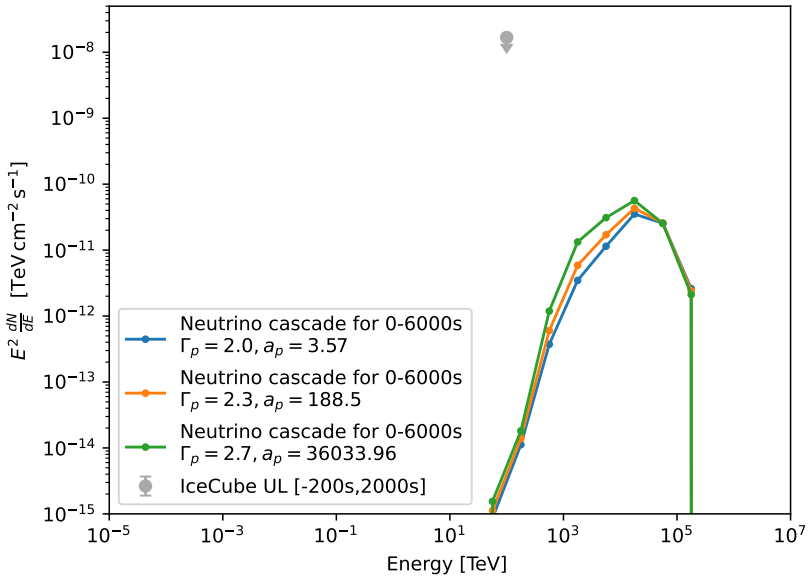


Figure 6.8: The obtained neutrino spectrum for the different 90% upper limit proton spectrum prefactors, assuming a magnetic field strength of $10^{-18}$ G. The high energy cut-off is set to $E_{cut} = 1 \cdot 10^{18}$ eV and the low energy cut-off to $E_{cut\_low} = 1 \cdot 10^{12}$ eV.

## 6.4 Late time observation

It is also possible to compare the spectra produced by the cascade with observations during later times. HESS observed GRB 221009A from $t_0 + 1.901 \cdot 10^5$ s until $t_0 + 7.122 \cdot 10^5$ s, where $t_0$ is the time of the Fermi GBM trigger. Additionally, the Fermi LAT data for that period were analysed in section 5.1.3 of this thesis. During these late times no primary spectrum contribution is expected. Hence, the only flux being observed at these times would come from the gamma rays produced in the cascades.

Figure 6.9 shows these observational data together with the cascade flux for the determined upper limits of the proton spectrum prefactor, assuming a magnetic field strength of $10^{-20}$ G. It can be seen in the figure that the cascade flux in the energy range of $1 \cdot 10^{-4}$ TeV $- 1 \cdot 10^{-3}$ TeV sometimes even lies above the obtained upper flux limits from Fermi LAT. Therefore the late-time observations might make it possible to set even stronger constraints on the proton spectrum cascades than the observation directly after the gamma-ray burst. However, since the observational data are very finely binned and show high variations between neighbouring bins in this energy range, a coarser energy binning might help to reduce these variations and help to draw better conclusions from the comparison of the Fermi LAT data and the the simulation data.

Figure 6.9 shows these observational data together with the cascade flux for the de-

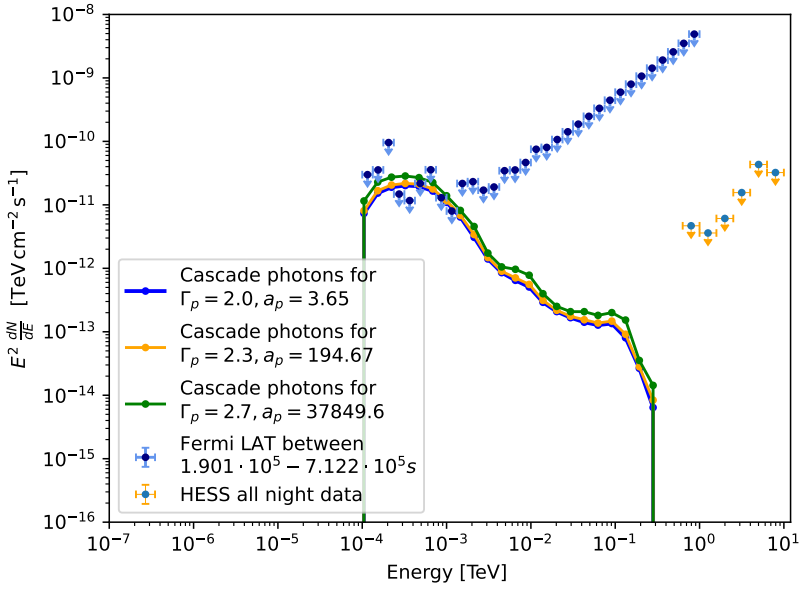


Figure 6.9: The obtained gamma-ray spectrum for an observation period between $t_0 + 1.901 \cdot 10^5$ s and $t_0 + 7.122 \cdot 10^5$ s. The spectrum is calculated for the three different proton spectrum prefactors and spectral indices, assuming a magnetic field strength of $10^{-20}$ G.

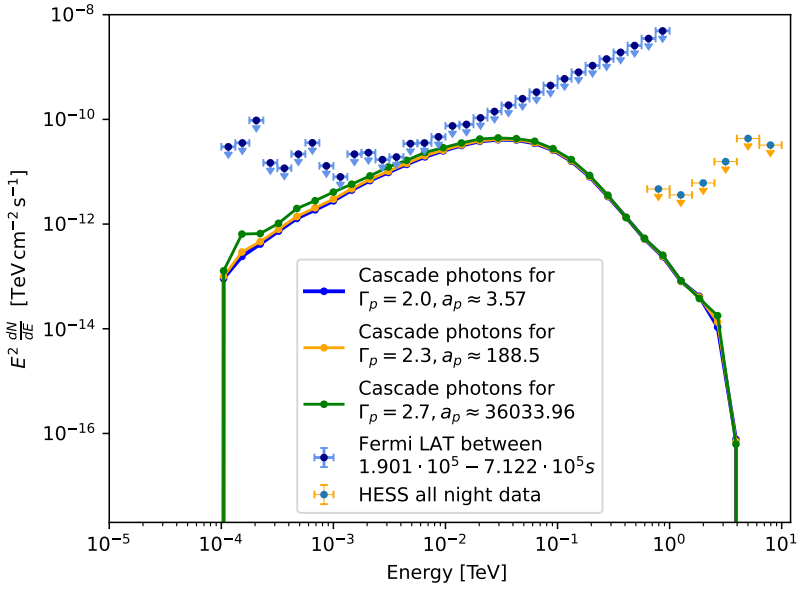


Figure 6.10: The obtained gamma-ray spectrum for an observation period between $t_0 + 1.901 \cdot 10^5$ s and $t_0 + 7.122 \cdot 10^5$ s. The spectrum is calculated for the three different proton spectrum prefactors and spectral indices, assuming a magnetic field strength of $10^{-18}$ G.

termined upper limits of the proton spectrum prefactor, assuming a magnetic field strength of $10^{-18}$ G. The cascade flux only shows small variations for the three cascade parameters. Additionally, for all three cases shown the cascade flux lies below the upper limits determined by Fermi LAT and HESS. Therefore the cascade flux obtained is consistent with observational limits. Comparing the spectrum between the different magnetic fields shows that for the higher magnetic fields, more highly energetic gamma-rays are expected from the cascades at these late observation times. This can be explained by the additional path length of the gamma rays, produced by deflected charged parent particles. For higher magnetic fields emitted gamma rays are expected to have on average a larger time delay and therefore the flux at higher energies at late observation times is higher for higher magnetic fields. For even higher than the considered magnetic fields, these higher fluxes at high energies might lead to conflicts, especially with the HESS observations. Hence, it would be interesting to perform simulations with higher magnetic fields.

# Chapter 7

# Summary & Outlook

In this thesis, the possible contribution of proton-induced cascades to the very high energy gamma-ray emission of GRB 221009A was studied.
Protons escaping the GRB can scatter with background radiation fields, inducing an electromagnetic cascade. The main scattering processes of these protons are for energies below the GZK cut-off Bethe-Heitler pair production and above the GZK cut-off photopion processes. The secondary particles produced in this way can afterward produce gamma rays through further processes. An example would be, that an electron created in a Bethe-Heitler process, afterward inverse Compton scatters with a photon from the EBL, producing a gamma ray. The gamma-ray flux measured by observatories directly after the GRB would therefore consist of two contributions: The primary gamma-ray emission directly from the GRB and a contribution from proton-induced cascades.
In the thesis numerical simulations, based on the CRPropa framework, were used to simulate those cascades produced by protons. These simulations yield a gamma-ray and neutrino flux that is compared to observational data.
The observed gamma-ray emission of GRB 221009A by KM2A and WCDA, between 300-900 s after the trigger by Fermi GBM are used to obtain an upper limit of the proton spectrum normalization for three assumed spectral indices of the protons spectrum.
These derived upper limits for the cascades prefactor were used to compare the neutrino emission produced by these cascades with neutrino flux upper limits derived from the non-observation of neutrinos by IceCube. The upper flux limits by IceCube are several orders of magnitude higher than the neutrino flux expected from the proton-induced cascades. Hence, the neutrino data give no further constraints on the proton spectrum.
Additionally, the derived proton spectrum prefactors were used to compare the expected gamma-ray flux by the cascades 2-9 days after the Fermi GBM trigger, with observations of the GRB by Fermi and HESS. Although both instruments did not de-

tect significant emission from the GRB, the derived upper limits, especially the ones by Fermi, seem to be a good starting point for further constraints on the proton spectrum. The secondary gamma-ray flux from the cascades assuming a magnetic field strength of $10^{-20}$ G is for some energies in conflict with the upper limits from Fermi, pointing towards stronger constraints. Because the spectral energy distribution obtained by Fermi is very narrowly binned and shows a high variations between neighbouring bins the significance of this conflict is limited and a coarser binning might help to draw better conclusions. Comparing the gamma-ray emission from the cascades at later times shows, that for stronger magnetic fields more high energy emission is expected at these observation times. This is caused by the deflection of the gamma-ray emitting charged particles, away from the line of sight, by the magnetic fields. These deflections increase the path length for secondary gamma-rays travelling to Earth, leading to a time delay compared to gamma rays that reach Earth directly. Especially for higher magnetic fields, this might set stronger constraints on the proton spectrum prefactor, as the later time gamma-ray flux from the cascades might challenge the observational upper limits.

The next step in interpreting the obtained upper limits of the proton spectrum prefactor is to calculate the proton luminosity. The proton luminosity is the isotropic equivalent energy of the cascade protons and, hence, a measure of the energy contained in the protons. This proton luminosity can be used to calculate the fraction of escaping protons. The ratio of the cascade proton luminosity found using the values obtained in this thesis and the total proton isotropic-equivalent luminosity will give an estimate of the proton escape fraction.

The gamma-ray emission from proton-induced cascades is just one of several possible theories explaining the detection of TeV gamma rays from GRB 221009A by LHAASO. Another potential explanation involves axion-like-particles. Axion-like-particles are hypothetical elementary particles that arise in theories beyond the standard model. These particles do not suffer from the EBL attenuation and could be created by photons in strong magnetic fields and, in the presence of the galactic magnetic fields, convert back to photons (Troitsky, 2022). Hence higher gamma-ray fluxes would be expected, making this an alternative explanation for the observations by LHAASO.

# Bibliography


Abbasi, R. et al. (Mar. 2023). "Limits on Neutrino Emission from GRB 221009A from MeV to PeV Using the IceCube Neutrino Observatory". In: *The Astrophysical Journal Letters* 946.1, p. L26. ISSN: 2041-8213. DOI: 10.3847/2041-8213/acc077. URL: http://dx.doi.org/10.3847/2041-8213/acc077.

Abbott, B. P. et al. (Oct. 2017). "Gravitational Waves and Gamma-Rays from a Binary Neutron Star Merger: GW170817 and GRB 170817A". In: *The Astrophysical Journal Letters* 848.2, p. L13. ISSN: 2041-8213. DOI: 10.3847/2041-8213/aa920c. URL: http://dx.doi.org/10.3847/2041-8213/aa920c.

Aharonian, F. et al. (Feb. 2021). "Observation of the Crab Nebula with LHAASO-KM2A - a performance study *". In: *Chinese Physics C* 45.2, p. 025002. ISSN: 2058-6132. DOI: 10.1088/1674-1137/abd01b. URL: http://dx.doi.org/10.1088/1674-1137/abd01b.

Aharonian, F. et al. (June 2023a). "Constraints on the Intergalactic Magnetic Field Using Fermi-LAT and H.E.S.S. Blazar Observations". In: *The Astrophysical Journal Letters* 950.2, p. L16. ISSN: 2041-8213. DOI: 10.3847/2041-8213/acd777. URL: http://dx.doi.org/10.3847/2041-8213/acd777.

Aharonian, F. et al. (Mar. 2023b). "H.E.S.S. Follow-up Observations of GRB 221009A". In: *The Astrophysical Journal Letters* 946.1, p. L27. ISSN: 2041-8213. DOI: 10.3847/2041-8213/acc405. URL: http://dx.doi.org/10.3847/2041-8213/acc405.

Alves Batista, Rafael et al. (Oct. 2016). "Probing intergalactic magnetic fields with simulations of electromagnetic cascades". In: *Phys. Rev. D* 94 (8), p. 083005. DOI: 10.1103/PhysRevD.94.083005. URL: https://link.aps.org/doi/10.1103/PhysRevD.94.083005.

Alves Batista, Rafael et al. (Sept. 2022). "CRPropa 3.2 — an advanced framework for high-energy particle propagation in extragalactic and galactic spaces". In: *Journal of Cosmology and Astroparticle Physics* 2022.09, p. 035. ISSN: 1475-7516. DOI: 10.1088/1475-7516/2022/09/035. URL: http://dx.doi.org/10.1088/1475-7516/2022/09/035.

Atwood, W. et al. (May 2009). "The Large Area Telescope on the Fermi Gamma-Ray Space Telescope Mission". In: *The Astrophysical Journal* 697, p. 1071. DOI: 10.1088/0004-637X/697/2/1071.

Berezinsky, Veniamin, Askhat Gazizov, and Svetlana Grigorieva (Aug. 2006). "On astrophysical solution to ultrahigh energy cosmic rays". In: *Physical Review D* 74.4. ISSN: 1550-2368. DOI: 10.1103/physrevd.74.043005. URL: http://dx.doi.org/10.1103/PhysRevD.74.043005.

Bissaldi, E. et al. (Oct. 2022). "GRB 221009A or Swift J1913.1+1946: Fermi-LAT detection". In: *GRB Coordinates Network* 32637, p. 1. URL: https://ui.adsabs.harvard.edu/abs/2022GCN.32637....1B.

Blumenthal, George R. and Robert J. Gould (Apr. 1970). "Bremsstrahlung, Synchrotron Radiation, and Compton Scattering of High-Energy Electrons Traversing Dilute Gases". In: *Rev. Mod. Phys.* 42 (2), pp. 237–270. DOI: 10.1103/RevModPhys.42.237. URL: https://link.aps.org/doi/10.1103/RevModPhys.42.237.

Bruel, P. (Dec. 2021). "A new method to perform data-model comparison in Fermi-LAT analysis". In: *Astronomy & Astrophysics* 656, A81. ISSN: 1432-0746. DOI: 10.1051/0004-6361/202141553. URL: http://dx.doi.org/10.1051/0004-6361/202141553.

Cao, Zhen et al. (2023a). "Very high energy gamma-ray emission beyond 10 TeV from GRB 221009A". In: *Sci. Adv.* 9.46, adj2778. DOI: 10.1126/sciadv.adj2778. arXiv: 2310.08845 [astro-ph.HE].

Cao, Zhen et al. (June 2023b). "A tera–electron volt afterglow from a narrow jet in an extremely bright gamma-ray burst". In: *Science* 380.6652, pp. 1390–1396. ISSN: 1095-9203. DOI: 10.1126/science.adg9328. URL: http://dx.doi.org/10.1126/science.adg9328.

Cerruti, Matteo (Oct. 2020). "Leptonic and Hadronic Radiative Processes in Supermassive-Black-Hole Jets". In: *Galaxies* 8.4, p. 72. ISSN: 2075-4434. DOI: 10.3390/galaxies8040072. URL: http://dx.doi.org/10.3390/galaxies8040072.

CRPropa Developers (n.d.). *CRPropa*. URL: https://crpropa.github.io/CRPropa3/index.html. (accessed: 08.12.2024).

Das, Saikat and Soebur Razzaque (Feb. 2023). "Ultrahigh-energy cosmic-ray signature in GRB 221009A". In: *Astronomy and Astrophysics* 670, p. L12. ISSN: 1432-0746. DOI: 10.1051/0004-6361/202245377. URL: http://dx.doi.org/10.1051/0004-6361/202245377.

de Ugarte Postigo, A. et al. (Oct. 2022). "GRB 221009A: Redshift from X-shooter/VLT". In: *GRB Coordinates Network* 32648, p. 1. URL: https://ui.adsabs.harvard.edu/abs/2022GCN.32648....1D.

Dembinski, Hans and Piti Ongmongkolkul et al. (Dec. 2020). "scikit-hep/iminuit". In: DOI: 10.5281/zenodo.3949207. URL: https://doi.org/10.5281/zenodo.3949207.

Dermer, Charles and Govind Menon (2009). *High-energy radiation from black holes gamma rays, cosmic rays, and neutrinos*. Princeton University Press.

Dichiara, S. et al. (Oct. 2022). "Swift J1913.1+1946 a new bright hard X-ray and optical transient". In: *GRB Coordinates Network* 32632, p. 1. URL: https://ui.adsabs.harvard.edu/abs/2022GCN.32632....1D.

Dwek, Eli and Frank Krennrich (Mar. 2013). "The extragalactic background light and the gamma-ray opacity of the universe". In: *Astroparticle Physics* 43, pp. 112–133. ISSN: 0927-6505. DOI: 10.1016/j.astropartphys.2012.09.003. URL: http://dx.doi.org/10.1016/j.astropartphys.2012.09.003.

Errando, Manel and Takayuki Saito (2023). "How to Detect Gamma Rays from Ground: An Introduction to the Detection Concepts". In: *Handbook of X-ray and Gamma-ray Astrophysics*. Springer Nature Singapore, pp. 1–37. ISBN: 9789811645440. DOI: 10.1007/978-981-16-4544-0_61-1. URL: http://dx.doi.org/10.1007/978-981-16-4544-0_61-1.

Essey, Warren et al. (Mar. 2011). "Role of line-of-sight cosmic ray interactions in forming the spectra of distant blazars in TeV gamma rays and high-energy neutrinos". In: *The Astrophysical Journal* 731.1, p. 51. ISSN: 1538-4357. DOI: 10.1088/0004-637x/731/1/51. URL: http://dx.doi.org/10.1088/0004-637X/731/1/51.

Fletcher, R. S., T. K. Gaisser, and F. Halzen (1994). "Muons in $\gamma$-ray Air Showers and the Photoproduction Cross Section". In: *Trends in Astroparticle-Physics*. Ed. by Peter Christian Bosetti. Wiesbaden: Vieweg+Teubner Verlag, pp. 179–187. ISBN: 978-3-663-01466-9. DOI: 10.1007/978-3-663-01466-9_16. URL: https://doi.org/10.1007/978-3-663-01466-9_16.

Fong, W. and E. Berger (Oct. 2013). "The Locations of Short Gamma-Ray Bursts as Evidence for Compact Object Binary Progenitors". In: *The Astrophysical Journal* 776.1, 18, p. 18. DOI: 10.1088/0004-637X/776/1/18. arXiv: 1307.0819 [astro-ph.HE].

Fruchter, A. S. et al. (May 2006). "Long $\gamma$-ray bursts and core-collapse supernovae have different environments". In: *Nature* 441.7092, pp. 463–468. ISSN: 1476-4687. DOI: 10.1038/nature04787. URL: http://dx.doi.org/10.1038/nature04787.

Funk, Stefan (Oct. 2015). "Ground- and Space-Based Gamma-Ray Astronomy". In: *Annual Review of Nuclear and Particle Science* 65, pp. 245–277. DOI: 10.1146/annurev-nucl-102014-022036. arXiv: 1508.05190 [astro-ph.HE].

Ghisellini, Gabriele (2013). *Radiative Processes in High Energy Astrophysics*. 1st ed. Springer Cham. ISBN: 978-3-319-00612-3. DOI: https://doi.org/10.1007/978-3-319-00612-3.

Goodman, J. (Sept. 1986). "Are gamma-ray bursts optically thick?" In: *Astrophysical Journal Letters* 308, p. L47. DOI: 10.1086/184741.

Greisen, Kenneth (Apr. 1966). "End to the Cosmic-Ray Spectrum?" In: *Phys. Rev. Lett.* 16 (17), pp. 748–750. DOI: 10.1103/PhysRevLett.16.748. URL: https://link.aps.org/doi/10.1103/PhysRevLett.16.748.

H.E.S.S. Collaboration (n.d.). *Auxiliary Information on results for the paper "H.E.S.S. follow-up observations of GRB 221009A"*. URL: https://www.mpi-hd.mpg.de/hfm/HESS/pages/publications/auxiliary/2023_GRB_221009A/. (accessed:21.12.2024).

H.E.S.S. collaboration (n.d.). *The H.E.S.S. Telescopes*. URL: https://www.mpi-hd.mpg.de/HESS/pages/about/. (accessed: 28.12.24).

Halzen, Francis and Spencer R. Klein (Aug. 2010). "Invited Review Article: IceCube: An instrument for neutrino astronomy". In: *Review of Scientific Instruments* 81.8, p. 081101. ISSN: 0034-6748. DOI: 10.1063/1.3480478. eprint: https://pubs.aip.org/aip/rsi/article-pdf/doi/10.1063/1.3480478/15900340/081101_1_online.pdf. URL: https://doi.org/10.1063/1.3480478.

Hinton, J.A. and W. Hofmann (2009). "Teraelectronvolt Astronomy". In: *Annual Review of Astronomy and Astrophysics* 47.Volume 47, 2009, pp. 523–565. ISSN: 1545-4282. DOI: https://doi.org/10.1146/annurev-astro-082708-101816. URL: https://www.annualreviews.org/content/journals/10.1146/annurev-astro-082708-101816.

IceCube (n.d.). *IceCube*. URL: https://icecube.wisc.edu/science/icecube/. (accessed: 29.12.2024).

Jackson, J D (1962). *Classical Electrodynamics*. 1st ed. Wiley R Sons Inc.

Kouveliotou, Chryssa et al. (Aug. 1993). "Identification of Two Classes of Gamma-Ray Bursts". In: *Astrophysical Journal Letters* 413, p. L101. DOI: 10.1086/186969.

Kumar, Pawan and Bing Zhang (Feb. 2015). "The physics of gamma-ray bursts and relativistic jets". In: *Physics Reports* 561, pp. 1–109. ISSN: 0370-1573. DOI: 10.1016/j.physrep.2014.09.008. URL: http://dx.doi.org/10.1016/j.physrep.2014.09.008.

Lesage, S. et al. (Aug. 2023). "Fermi-GBM Discovery of GRB 221009A: An Extraordinarily Bright GRB from Onset to Afterglow". In: *The Astrophysical Journal Letters* 952.2, p. L42. DOI: 10.3847/2041-8213/ace5b4. URL: https://dx.doi.org/10.3847/2041-8213/ace5b4.

LHAASO collaboration (2021). *Performance of LHAASO-WCDA and Observation of Crab Nebula as a Standard Candle*. arXiv: 2101.03508 [astro-ph.IM]. URL: https://arxiv.org/abs/2101.03508.

Longair, Malcolm S. (2011). *High Energy Astrophysics*. 3rd ed. Cambridge University Press. DOI: https://doi.org/10.1017/CBO9780511778346.

Madejski, Grzegorz (Greg) and Marek Sikora (2016). "Gamma-Ray Observations of Active Galactic Nuclei". In: *Annual Review of Astronomy and Astrophysics* 54.Volume 54, 2016, pp. 725–760. ISSN: 1545-4282. DOI: https://doi.org/10.1146/annurev-astro-081913-040044. URL: https://www.annualreviews.org/content/journals/10.1146/annurev-astro-081913-040044.

Matthews, J. (2005). "A Heitler model of extensive air showers". In: *Astroparticle Physics* 22.5, pp. 387–397. ISSN: 0927-6505. DOI: https://doi.org/10.1016/j.astropartphys.2004.09.003. URL: https://www.sciencedirect.com/science/article/pii/S0927650504001598.

Meegan, Charles et al. (Aug. 2009). "The Fermi Gamma-Ray Burst Monitor". In: *The Astrophysical Journal* 702.1, pp. 791–804. ISSN: 1538-4357. DOI: 10.1088/0004-637x/702/1/791. URL: http://dx.doi.org/10.1088/0004-637X/702/1/791.

NASA (Nov. 2018). *Likelihood Overview*. URL: https://fermi.gsfc.nasa.gov/ssc/data/analysis/documentation/Cicerone/Cicerone_Likelihood/Likelihood_overview.html. (accessed: 21.12.2024).

– (n.d.[a]). *LAT Data Selection Recommendations*. URL: https://fermi.gsfc.nasa.gov/ssc/data/analysis/documentation/Cicerone/Cicerone_Data_Exploration/Data_preparation.html. (accessed: 31.05.2024).

– (n.d.[b]). *LAT Photon, Event, and Spacecraft Data Query*. URL: https://fermi.gsfc.nasa.gov/cgi-bin/ssc/LAT/LATDataQuery.cgi. (accessed: 19.07.2024).

NASA's Goddard Space Flight Center (n.d.). URL: https://www.nasa.gov/universe/nasa-missions-study-what-may-be-a-1-in-10000-year-gamma-ray-burst/. (accessed: 20.11.24).

NASA's Goddard Space Flight Center and Adam Goldstein (USRA) (n.d.). URL: https://www.nasa.gov/universe/nasa-missions-study-what-may-be-a-1-in-10000-year-gamma-ray-burst/. (accessed: 20.11.24).

Omodei, N. et al. (Oct. 2022). "GRB 221009A: Fermi LAT data rate effects due to extremely high flux". In: *GRB Coordinates Network* 32760, p. 1. URL: https://ui.adsabs.harvard.edu/abs/2022GCN.32760....1O.

Paczynski, B. (Sept. 1986). "Gamma-ray bursters at cosmological distances". In: *Astrophysical Journal Letters* 308, pp. L43–L46. DOI: 10.1086/184740.

Piran, Tsvi (June 1999). "Gamma-ray bursts and the fireball model". In: *Physics Reports* 314.6, pp. 575–667. DOI: 10.1016/S0370-1573(98)00127-6. arXiv: astro-ph/9810256 [astro-ph].

– (Jan. 2005). "The physics of gamma-ray bursts". In: *Rev. Mod. Phys.* 76 (4), pp. 1143–1210. DOI: 10.1103/RevModPhys.76.1143. URL: https://link.aps.org/doi/10.1103/RevModPhys.76.1143.

Rudolph, Annika et al. (Feb. 2023). "Multi-messenger Model for the Prompt Emission from GRB 221009A". In: *The Astrophysical Journal Letters* 944.2, p. L34. ISSN: 2041-8213. DOI: 10.3847/2041-8213/acb6d7. URL: http://dx.doi.org/10.3847/2041-8213/acb6d7.

Saldana-Lopez, Alberto et al. (Aug. 2021). "An observational determination of the evolving extragalactic background light from the multiwavelength HST/CANDELS survey in the Fermi and CTA era". In: *Monthly Notices of the Royal Astronomical*

*Society* 507.4, pp. 5144–5160. ISSN: 0035-8711. DOI: 10.1093/mnras/stab2393. eprint: https://academic.oup.com/mnras/article-pdf/507/4/5144/40391540/stab2393.pdf. URL: https://doi.org/10.1093/mnras/stab2393.

Sari, Re'em and Ann A. Esin (Feb. 2001). "On the Synchrotron Self-Compton Emission from Relativistic Shocks and Its Implications for Gamma-Ray Burst Afterglows". In: *The Astrophysical Journal* 548.2, p. 787. DOI: 10.1086/319003. URL: https://dx.doi.org/10.1086/319003.

Shemi, Amotz and Tsvi Piran (Dec. 1990). "The Appearance of Cosmic Fireballs". In: *Astrophysical Journal Letters* 365, p. L55. DOI: 10.1086/185887.

Troitsky, S. V. (Nov. 2022). "Parameters of Axion-Like Particles Required to Explain High-Energy Photons from GRB 221009A". In: *JETP Letters* 116.11, pp. 767–770. ISSN: 1090-6487. DOI: 10.1134/s0021364022602408. URL: http://dx.doi.org/10.1134/S0021364022602408.

Veres, P. et al. (Oct. 2022). "GRB 221009A: Fermi GBM detection of an extraordinarily bright GRB". In: *GRB Coordinates Network* 32636, p. 1. URL: https://ui.adsabs.harvard.edu/abs/2022GCN.32636....1V.

Wood, Matthew et al. (2017). *Fermipy: An open-source Python package for analysis of Fermi-LAT Data*. arXiv: 1707.09551 [astro-ph.IM]. URL: https://arxiv.org/abs/1707.09551.

Woosley, Stan (Dec. 2001). "Blinded by the light". In: *Nature* 414.6866, pp. 853–854. DOI: 10.1038/414853a. URL: https://doi.org/10.1038/414853a.

Zhang, Bing (2018). *The Physics of Gamma-Ray Bursts*. Cambridge University Press.

Zuo, Xiong et al. (2015). "Design and performances of prototype muon detectors of LHAASO-KM2A". In: *Nuclear Instruments and Methods in Physics Research Section A: Accelerators, Spectrometers, Detectors and Associated Equipment* 789, pp. 143–149. ISSN: 0168-9002. DOI: https://doi.org/10.1016/j.nima.2015.04.010. URL: https://www.sciencedirect.com/science/article/pii/S0168900215004696.

# Appendix A

# Appendix

## A.1 Comparing to LHAASO data

### Cascade not fully fixed

| Name | Value | Hesse Err | Limit- | Limit+ | Fixed |
|---|---|---|---|---|---|
| A | 2.1068e-7 | 0.0000e-7 | 0 | | |
| $\Gamma$ | 2.3103 | 0.0000 | 1.5 | 4.0 | |
| $a_p$ | 0.0 | 0.1 | 0 | | yes |
| $\Gamma_p$ | 2 | 0 | 1 | 4 | |
| $E_{cut}$ | 10e17 | 0e17 | 1e+17 | 1e+18 | |
| $E_{cut\_low}$ | 1.00e12 | 0.01e12 | 0 | | yes |

Table A.1: Best fit parameters for nearly all cascade parameters free for $A_p = 0.0$, $\chi^2 = 46.6$

| Name | Value | Hesse Err | Limit- | Limit+ | Fixed |
|---|---|---|---|---|---|
| A | 211e-9 | 5e-9 | 0 | | |
| $\Gamma$ | 2.310 | 0.022 | 1.5 | 4.0 | |
| $a_p$ | 1.00e-3 | 0.01e-3 | 0 | | yes |
| $\Gamma_p$ | 2.1 | 2.5 | 1 | 4 | |
| $E_{cut}$ | 0.1e18 | 0.8e18 | 1e+17 | 1e+18 | |
| $E_{cut\_low}$ | 1.00e12 | 0.01e12 | 0 | | yes |

Table A.2: Best fit parameters for nearly all cascade parameters free for $a_p = 1.00 \cdot 10^{-3}$, $\chi^2 = 46.6$

| Name | Value | Hesse Err | Limit- | Limit+ | Fixed |
|---|---|---|---|---|---|
| A | 211e-9 | 5e-9 | 0 | | |
| $\Gamma$ | 2.310 | 0.022 | 1.5 | 4.0 | |
| $a_p$ | 1.00 | 0.01 | 0 | | yes |
| $\Gamma_p$ | 2.3 | 2.3 | 1 | 4 | |
| $E_{cut}$ | 0.1e18 | 0.6e18 | 1e+17 | 1e+18 | |
| $E_{cut\_low}$ | 1.00e12 | 0.01e12 | 0 | | yes |

Table A.3: Best fit parameters for nearly all cascade parameters free for $a_p = 1.0$, $\chi^2 = 46.6$

| Name | Value | Hesse Err | Limit- | Limit+ | Fixed |
|---|---|---|---|---|---|
| A | 211e-9 | 4e-9 | 0 | | |
| $\Gamma$ | 2.310 | 0.021 | 1.5 | 4.0 | |
| $a_p$ | 10.0 | 0.1 | 0 | | yes |
| $\Gamma_p$ | 2.6 | 1.8 | 1 | 4 | |
| $E_{cut}$ | 0.1e18 | 0.6e18 | 1e+17 | 1e+18 | |
| $E_{cut\_low}$ | 1.00e12 | 0.01e12 | 0 | | yes |

Table A.4: Best fit parameters for nearly all cascade parameters free for $a_p = 10.0$, $\chi^2 = 46.6$

| Name | Value | Hesse Err | Limit- | Limit+ | Fixed |
|---|---|---|---|---|---|
| A | 211e-9 | 5e-9 | 0 | | |
| $\Gamma$ | 2.310 | 0.022 | 1.5 | 4.0 | |
| $a_p$ | 100.0 | 1 | 0 | | yes |
| $\Gamma_p$ | 3 | 2 | 1 | 4 | |
| $E_{cut}$ | 0.1e18 | 0.5e18 | 1e+17 | 1e+18 | |
| $E_{cut\_low}$ | 1.00e12 | 0.01e12 | 0 | | yes |

Table A.5: Best fit parameters for nearly all cascade parameters free for $a_p = 100.0$, $\chi^2 = 46.6$

| Name | Value | Hesse Err | Limit- | Limit+ | Fixed |
|---|---|---|---|---|---|
| A | 211e-9 | 5e-9 | 0 | | |
| $\Gamma$ | 2.310 | 0.022 | 1.5 | 4.0 | |
| $a_p$ | 1.00e3 | 0.01e3 | 0 | | yes |
| $\Gamma_p$ | 3.0 | 2.4 | 1 | 4 | |
| $E_{cut}$ | 0.1e18 | 0.9e18 | 1e+17 | 1e+18 | |
| $E_{cut\_low}$ | 1.00e12 | 0.01e12 | 0 | | yes |

Table A.6: Best fit parameters for nearly all cascade parameters free for $a_p = 1000.0$, $\chi^2 = 46.6$

## Cascade fully fixed

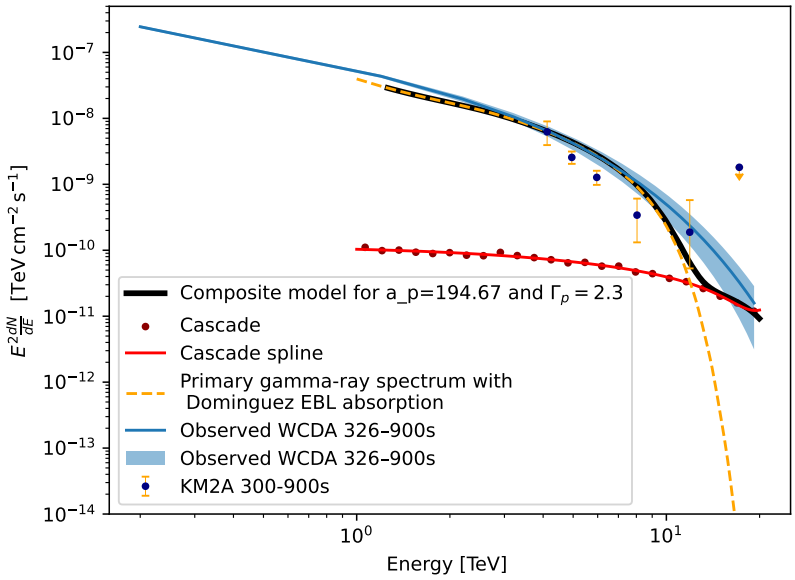


Figure A.1: The obtained spectrum for the 90% upper limit of the proton spectrum with spectral index of 2.3. It is plotted with the upper limit prefactor $a_p^{90\%} \approx 194.67$, $E_{cut} = 1 \cdot 10^{18}$ eV, $E_{cut\_low} = 1 \cdot 10^{12}$ eV, $A = 210 \cdot 10^{-9} \frac{1}{\text{TeV cm}^2 \text{ s}}$, $\Gamma = 2.313$, assuming a magnetic field strength of $10^{-20}$G.

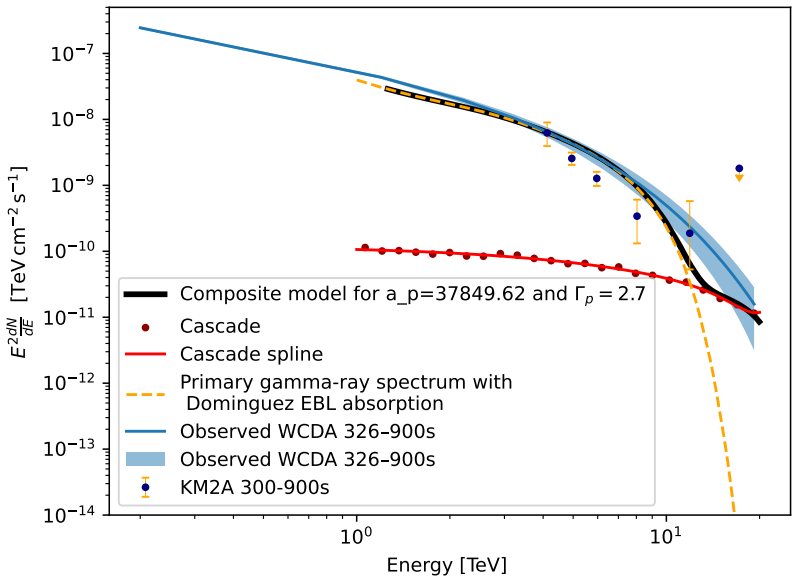


Figure A.2: The obtained spectrum for the 90% upper limit of the proton spectrum with spectral index of 2.7. It is plotted with the upper limit prefactor $a_p^{90\%} \approx 37849.62$, $E_{cut} = 1 \cdot 10^{18}$ eV, $E_{cut\_low} = 1 \cdot 10^{12}$ eV, $A = 210 \cdot 10^{-9} \frac{1}{\text{TeV cm}^2 \text{ s}}$, $\Gamma = 2.313$, assuming a magnetic field strength of $10^{-20}$G.

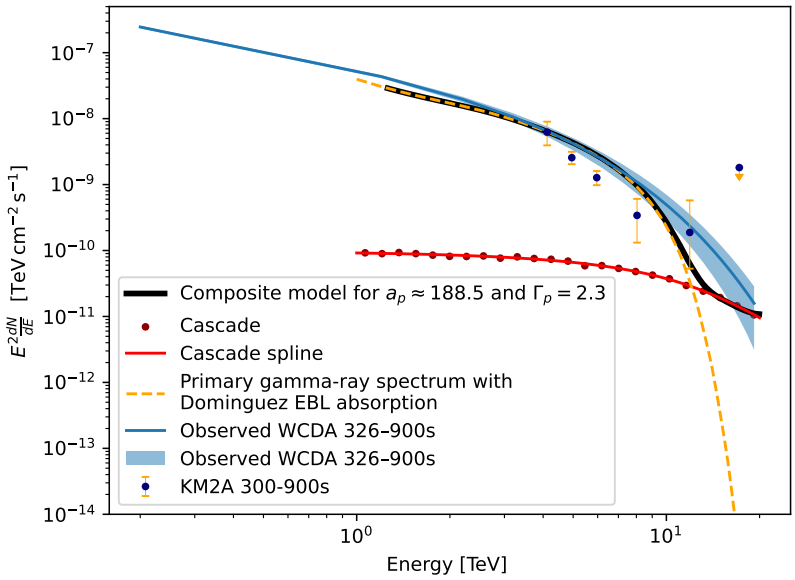


Figure A.3: The obtained spectrum for the 90% upper limit of the proton spectrum with spectral index of 2.7. It is plotted with the upper limit prefactor $a_p^{90\%} \approx 188.5$, $E_{cut} = 1 \cdot 10^{18}$ eV, $E_{cut\_low} = 1 \cdot 10^{12}$ eV, $A = 210 \cdot 10^{-9} \frac{1}{\text{TeV cm}^2 \text{ s}}$, $\Gamma = 2.313$, assuming a magnetic field strength of $10^{-18}$G.

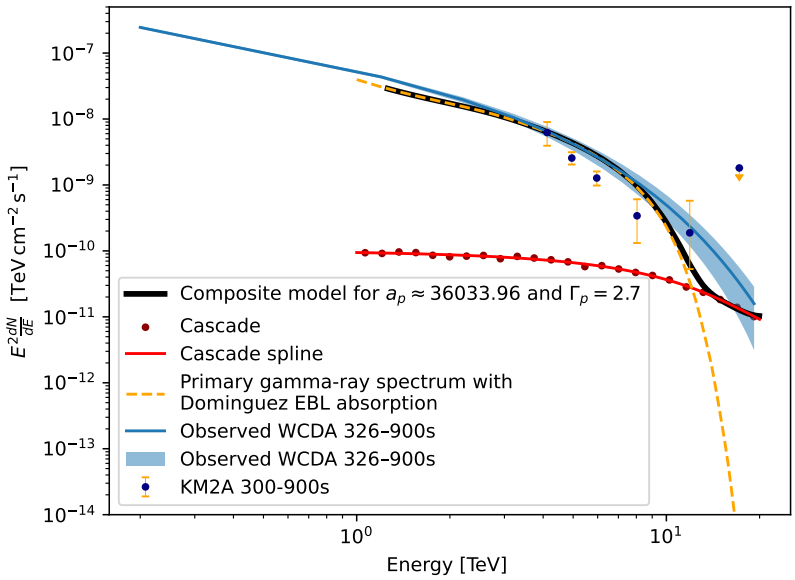


Figure A.4: The obtained spectrum for the 90% upper limit of the proton spectrum with spectral index of 2.7. It is plotted with the upper limit prefactor $a_p^{90\%} \approx 36033.96$, $E_{cut} = 1 \cdot 10^{18}$ eV, $E_{cut\_low} = 1 \cdot 10^{12}$ eV, $A = 210 \cdot 10^{-9}$ $\frac{1}{\text{TeV cm}^2\text{ s}}$, $\Gamma = 2.313$, assuming a magnetic field strength of $10^{-18}$G.